Journal Pre-proof

Real-time tomographic diffraction imaging of catalytic membrane reactors for the oxidative coupling of methane

Antonis Vamvakeros, Dorota Matras, Simon D.M. Jacques, Marco di Michiel, Vesna Middelkoop, Peixi Cong, Stephen W.T. Price, Craig L. Bull, Pierre Senecal, Andrew M. Beale

PII: S0920-5861(20)30337-0

DOI: https://doi.org/10.1016/j.cattod.2020.05.045

Reference: CATTOD 12895

To appear in: *Catalysis Today*

Received Date: 12 October 2019

Revised Date: 28 January 2020

Accepted Date: 14 May 2020

Please cite this article as: Vamvakeros A, Matras D, Jacques SDM, di Michiel M, Middelkoop V, Cong P, Price SWT, Bull CL, Senecal P, Beale AM, Real-time tomographic diffraction imaging of catalytic membrane reactors for the oxidative coupling of methane, *Catalysis Today* (2020), doi: https://doi.org/10.1016/j.cattod.2020.05.045

This is a PDF file of an article that has undergone enhancements after acceptance, such as the addition of a cover page and metadata, and formatting for readability, but it is not yet the definitive version of record. This version will undergo additional copyediting, typesetting and review before it is published in its final form, but we are providing this version to give early visibility of the article. Please note that, during the production process, errors may be discovered which could affect the content, and all legal disclaimers that apply to the journal pertain.

© 2020 Published by Elsevier.

Journal Pre-proof

Real-time tomographic diffraction imaging of catalytic membrane reactors for the oxidative coupling of methane

Antonis Vamvakeros[1,2,3*], Dorota Matras[2,3,4], Simon D. M. Jacques[3*], Marco di Michiel[5], Vesna Middelkoop[6], Peixi Cong[1,2], Stephen W. T. Price[3], Craig L. Bull[7], Pierre Senecal[1,2] and Andrew M. Beale[1,2,3*]

1 Department of Chemistry, University College London, 20 Gordon Street, London, WC1H 0AJ, UK.

2 Research Complex at Harwell, Harwell Science and Innovation Campus, Rutherford Appleton Laboratory, Didcot, Oxon, OX11 0FA, UK.

3 Finden Limited, Merchant House, 5 East St Helen Street, Abingdon, OX14 5EG, UK.

4 School of Materials, University of Manchester, Manchester, Lancashire M13 9PL, UK.

5 ESRF- The European Synchrotron, Grenoble, 38000 France.

6 Flemish Institute for Technological Research, VITO NV, Boeretang 200, 2400 Mol, Belgium.

7 ISIS Neutron and Muon Source, Rutherford Appleton Laboratory, Didcot, OX11 0QX, UK.

Correspondence email: antony@finden.ac.uk, simon@finden.ac.uk, andrew.beale@ucl.ac.uk

Graphical Abstract

Journal Pre-proof

Journal Pre-proof

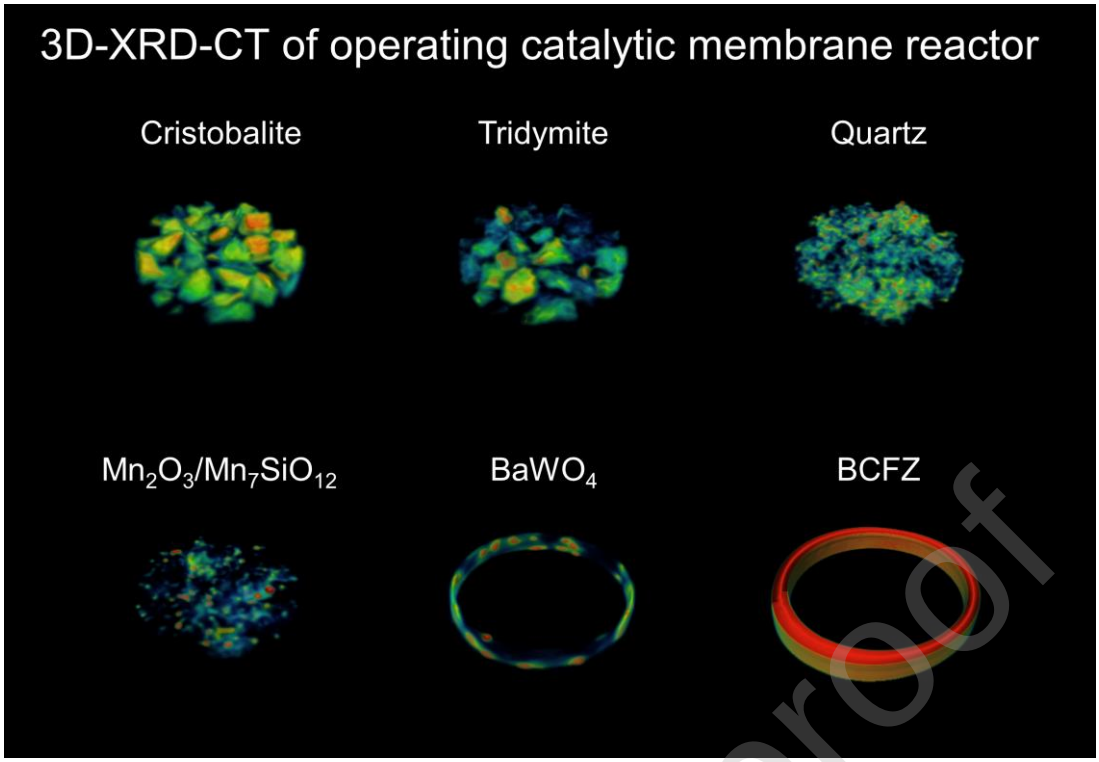

Highlights

- Synchrotron X-ray diffraction computed tomography applied to three fixed bed catalytic membrane reactors
- The solid-state evolution of catalysts and membranes is tracked under operating conditions
- A new crystal structure model of $BaCo_{0.4}Fe_{0.4}Zr_{0.2}O_{3-\delta}$ (BCFZ) is suggested and used for diffraction data analysis

Abstract

Catalytic membrane reactors have the potential to render the process of oxidative coupling of methane economically viable. Here, the results from operando XRD-CT studies of three different catalytic membrane reactors, employing

Journal Pre-proof

$BaCo_{0.4}Fe_{0.4}Zr_{0.2}O_{3-\delta}$ (BCFZ) and $La_{0.6}Sr_{0.4}Co_{0.2}Fe_{0.8}O_{3-\delta}$ (LSCF) perovskite membranes with Mn-Na-W/SiO_2 and La-promoted Mn-Na-W/SiO_2 catalysts, are presented. It is shown that synchrotron X-ray tomographic diffraction imaging allows the extraction of spatially-resolved diffraction information from the interior of these working catalytic membrane reactors and makes it possible to capture the evolving solid-state chemistry of their components under various operating conditions (i.e. temperature and chemical environment).

Introduction

In the past decade, the advances achieved in shale gas extraction, coupled with the continuous global effort to reduce and ban gas flaring, have led to dramatic increases in methane availability [1,2]. Methane is nowadays considered to be an abundant hydrocarbon source and, it being the main component of natural gas, much cheaper than crude oil [3]. These developments have set a strong economic imperative towards the utilisation of methane for the direct production of more precious light olefins and other bulk chemicals [4]. A characteristic example is the direct conversion of methane, under the presence of oxygen, to ethylene which is one of the most important building blocks used in the chemical industry [5]. This approach, known as the oxidative coupling of methane (OCM) reaction, is an alternative to the conventional energy-intensive naphtha steam cracking [6]. Historically, this reaction has been mainly studied using fixed bed reactor configuration but as in the case of many selective oxidation reactions, there is a trade-off between selectivity and yield for the desired product molecule (ethylene).

In the past two decades, there has been considerable effort in exploring alternative reactor designs as a means to reach a stable 30 % yield for C_2 molecules (i.e. ethane and ethylene) which is often reported as the target goal for this technology [7]. Among the various reactor types, it has been realised that those incorporating membranes, which act as oxygen distributors to the catalyst bed, hold a lot of potential [8–11]. The OCM reaction typically takes place at high temperatures (i.e. > 750 °C) and for this reason most often perovskite-type materials are employed [12–16]. These have mixed ionic and electronic conducting properties (MIEC materials)

Journal Pre-proof

and activate at temperatures similar to the operating ones required for the OCM reaction [17]. The MIEC materials are in the form of dense ceramic membranes allowing only oxygen anionic species to diffuse through them, therefore exhibiting pure permeation selectivity for the desired molecules [18,19]. Several geometries have been developed over the past two decades but the one attracting the most interest is the hollow-fibre geometry due to the very large active surface area (i.e. area-to-volume ratio in the range of 500–9000 m^2/m^3) [20,21]. The incorporation of dense hollow-fibre perovskite-type membranes in the catalytic processes, especially for the OCM reaction, shows several advantages when compared to conventional reactor configurations [21–26]:

- Maintaining the oxygen partial pressure (pO_2) low and homogeneously distributing the oxygen over the chemical reactor can lead to an increase in C_2 selectivity by preventing the total oxidation of methane. The uniform distribution of oxygen mitigates reaction rate and selectivity gradients along the reactor, both of which cannot be avoided in fixed bed reactors.

- Process Intensification: The oxygen separation unit (i.e. separation of oxygen from air) is no longer needed which increases the energy efficiency and decreases the cost of the overall process.

- The formation of NO_x is avoided as the membrane is selective only for oxygen. The risk of having explosive mixtures is also reduced and higher productivity can be achieved compared to fixed bed reactors as the ratio of the reactants can be closer to stoichiometry.

- The formation of hot spots (common problem in fixed bed reactors) can be mitigated due to the gradual feeding of oxygen along the reactor.

Two of the most promising MIEC membranes investigated as part of membrane reactors for the OCM reaction are $La_{0.6}Sr_{0.4}Co_{0.8}Fe_{0.2}O_{3-\delta}$ (LSCF) and $BaCo_{0.4}Fe_{0.4}Zr_{0.2}O_{3-\delta}$ (BCFZ) [27–30]. These membranes have been also coupled with catalyst fixed beds in catalytic membrane reactor configurations. However, these complex integrated reactor systems are conventionally characterised ex situ (i.e. before and after an OCM experiment) with destructive local probing characterisation

Journal Pre-proof

techniques (e.g. electron microscopy coupled with elemental analysis) or global probing techniques after sample treatment (e.g. sample grinding for bulk ex situ or in situ powder diffraction). These approaches can provide some information regarding the stability of the various material systems but offer little in terms of understanding their real active state and behaviour under OCM operating conditions or complex chemical environments [25,31–39].

Synchrotron X-ray based techniques have the potential to bridge this operando gap often present in catalytic membrane reactor experiments [40,41]. The brilliant X-rays generated at third generation synchrotrons allow the investigation of multi-component systems under real processing conditions which can help us gain a better understanding of their behaviour under different operating conditions [42–46]. As an example, it is possible to investigate under which conditions the MIEC materials undergo phase transformations, form carbonate layers, or what is the state of the catalyst bed in a membrane reactor compared to a fixed bed one; questions often left unanswered with conventional ex situ characterisation. On the other hand, synchrotron-based X-ray chemical tomography techniques can provide this information and also in a spatially-resolved manner [43-61]. We previously employed X-ray diffraction computed tomography (XRD-CT) to study a BCFZ hollow-fibre membrane combined with a Mn-Na-W/SiO_2 catalyst demonstrating for the first time the feasibility of such experiments [66–68]. In this work, we performed a thorough investigation of three catalytic membrane reactors investigating the behaviour of the various reactor components under different operating conditions (i.e. temperature and chemical environment).

Materials and Methods

Catalyst and Membrane preparation

The 2 wt. % La – 2 wt. % Mn – 1.6 wt. % Na – 3.1 wt. %W/SiO_2 and the 2 wt. % Mn – 1.6 wt. % Na – 3.1 wt. % W/SiO_2 catalysts were prepared by the sequential incipient wetness impregnation method [69,70]. At first a SiO_2 support (commercial Silica gel Davisil 646) was impregnated by an aqueous solution of sodium tungstate dehydrate $Na_2WO_4 \bullet 2H_2O$ and sodium oxalate $Na_2C_2O_4$ taken in appropriate amounts. The Na-

Journal Pre-proof

W/SiO_2 was dried at 120 °C for 6 h and was then impregnated by an aqueous solution of manganese (II) acetate tetrahydrate $Mn(CH_3COO)_2 \bullet 4H_2O$ and lanthanum nitrate hexahydrate $La(NO_3)_3 \bullet 6H_2O$ salts, taken in appropriate concentrations. The catalysts were then dried at 120 °C for 6 h and calcined in air at 850 °C for 6 h with a heating rate of 2 °C min^{-1}. Each catalyst sample was sieved obtaining a size fraction of 250-500 µm. The catalysts used in this study were kindly provided by the Boreskov Institute of Catalysis.

The ceramic powders used for the membrane production were fabricated by spray pyrolysis by CerPoTech AS (Trondheim, Norway). Aqueous solutions of the respective precursors were prepared and mixed in stoichiometric ratios, before the stable solution was sprayed into a furnace for each material. The as-prepared powders were calcined, ball milled in ethanol with YSZ grinding media and sieved, before a final heat treatment was executed to remove organic residues from powder processing. The $BaCo_{0.4}Fe_{0.4}Zr_{0.2}O_{3-\delta}$ and $La_{0.6}Sr_{0.4}Co_{0.2}Fe_{0.8}O_{3-\delta}$ (LSCF) membranes reported here have been manufactured using the spinning and phase inversion methods [71,72]. The starting polymer suspension was prepared from cellulose acetate (CA, Mr ~52000, Fluka), dimethylsulphoxide (DMSO, Synthesis grade, Merck) and de-ionised water that were used as a phase-inversion polymer, solvent and non-solvent additive to the polymer solution, respectively. The ceramic hollow-fibre membranes used in this study were kindly provided by the Flemish Institute for Technological Research (VITO).

Operando XRD-CT measurements at ID15A, ESRF

XRD-CT measurements were made at beamline station ID15A of the ESRF using a 92.8 keV monochromatic X-ray beam focused to have a spot size of 25 µm x 25 µm. 2D powder diffraction patterns were collected using a Pilatus3 X CdTe 300K (487 × 619 pixels, pixel size of 172 µm) hybrid photon counting area detector which uses Cadmium Telluride (CdTe) as the semiconducting direct conversion layer. The acquisition time per point was 50 ms. The tomographic measurements were made with 140 translation steps (translation step size of 25 µm) covering 0 – 180 ° angular range, in steps of 1.8 ° (i.e. 100 line scans). The total acquisition time for each XRD-CT dataset was ca. 25 min. The detector calibration was performed using a CeO_2 NIST standard. Every 2D diffraction image was converted to a 1D powder diffraction

Journal Pre-proof

pattern after applying an appropriate filter (i.e. 10 % trimmed mean filter) to remove outliers using in-house developed MATLAB scripts [73]. The final XRD-CT images (i.e. reconstructed data volume) were reconstructed using the filtered back projection algorithm.

Reactor Cells

Three types of catalytic membrane reactors suitable for the oxidative coupling of methane were prepared from hollow-fibre membranes (ca. 2.4 mm Ø and 180 µm wall thickness) packed with a catalyst supported between glass wool. More specifically, the following CMRs were tested: 1) BCFZ membrane with Mn-Na-W/SiO_2 catalyst, 2) BCFZ membrane with La-Mn-Na-W/SiO_2 catalyst and 3) LSCF membrane with La-Mn-Na-W/SiO_2 catalyst. The catalyst loading in each CMR was ca. 30 mg. In every experiment, the catalytic membrane reactor was glued on top of an alumina rod. For the operando XRD-CT experiments, the reactor cell (i.e. the CMR and the alumina rod) was inserted inside a quartz glass tube and a Swagelok union cross was used to allow the use of two different gas streams (see Figures S1 and S2). Dry air and pure gases of CH_4 and He were delivered to the reactor by GF40 Brooks mass flow controllers. Air was used at the outer side of the membrane and a mixture of CH_4 diluted in He at the inner side of the membrane. The values for the flow rates reported throughout the text correspond to close to NTP (normal temperature and pressure, 20 °C and 1 atm, respectively).

In each experiment, the reactor was mounted into a gas delivery stub, itself mounted to a standard goniometer (to enable alignment). The goniometer was fixed to a rotation stage set upon a translation stage to facilitate the movements required for the CT measurement. Heating was achieved by virtue of two hot air blowers (Cyberstar) heating each side of the catalytic reactor to ensure homogeneous temperature distribution over the CMR [74]. The hot air blowers were mounted on the translation stage and were moving with the reactor during the translation scans, maintaining the hot air blowers-to-reactor distance constant. XRD-CT measurements were performed at nominal temperatures, ambient up to 1000 °C equating to actual temperatures (i.e. after temperature calibration) of ambient and 780 °C with a nominal ramp rate of 10 °C min^{-1}. Temperature calibration of the heating system was

Journal Pre-proof

performed prior to the OCM experiments (Figure S3). During the operando XRD-CT measurements, the outflow gasses were monitored by mass spectrometry using an Ecosys portable mass spectrometer. The mass spec line was inserted inside the membrane from the top.

Rietveld analysis of the XRD-CT data

Rietveld analysis was performed using the reconstructed diffraction patterns with the TOPAS software, on a voxel by voxel basis [75]. The results from the Rietveld analysis of the XRD-CT data were imported into MALTAB in order to create the figures presented in this study (e.g. phase distribution maps based on the scale factors, unit cell parameters maps, etc.)[76]. The Rietveld analysis of the XRD-CT data was mainly based on the intensity of the scale factors (unless stated otherwise) and should be treated as a semi-quantitative analysis. In order to have a good starting model, quantitative Rietveld analysis of the summed diffraction pattern of all XRD-CT datasets was performed prior to the Rietveld analysis of the XRD-CT data.

It is important to note that prior to the reconstruction of the XRD-CT images and their analysis several issues needed to be addressed, including self-absorption artefacts and the creation of a crystal structure model for the BCFZ phase. A detailed description of the self-absorption correction strategy used in this work and the BCFZ crystal structure model refined using combined neutron and X-ray powder diffraction data is provided in the Supporting Information (Figures S2-6 and S7-13 respectively).

Results & Discussion

Operando XRD-CT measurements of CMRs during OCM

BCFZ membrane with Mn-Na-W/SiO2 catalyst

A schematic representation of the experimental protocol followed for the OCM experiment with the BCFZ – 2 % Mn – 1.6 % Na – 3.1 % W/SiO_2 CMR is shown in Figure 1. XRD-CT measurements were made at nominal temperatures, ambient, 800, 900 and 1000 °C equating to actual temperatures (i.e. after temperature calibration) of ca. ambient, 660, 720 and 780 °C. The temperature of the system was increased with a ramp rate of 5 °C min^{-1} under the flow of He. More specifically, 30 ml min^{-1} He flow

Journal Pre-proof

rate was used at the inner side of the membrane through the catalyst bed and 30 ml min^{-1} air flow at the outer side of the membrane. After reaching the required temperature for the OCM experiment (i.e. 780 °C), air was used from both sides of the BCFZ membrane as an activation step before switching to OCM conditions (i.e. flow rate of 50 ml min^{-1}). Next, different OCM reaction mixtures were used by varying the concentration of CH_4 in He (i.e. 5, 20, 50 and 100 % CH_4 in He). 3D-XRD-CT was then performed by collecting 11 XRD-CT 'slices' at different positions along the reactor (i.e. 25 µm apart) while keeping the reaction mixture the same (i.e. 100 ml min^{-1} of CH_4 at the inner side of the membrane through the catalyst bed and 100 ml min^{-1} air at the outer side of the membrane). The system was then cooled to room temperature and a final XRD-CT dataset was collected.

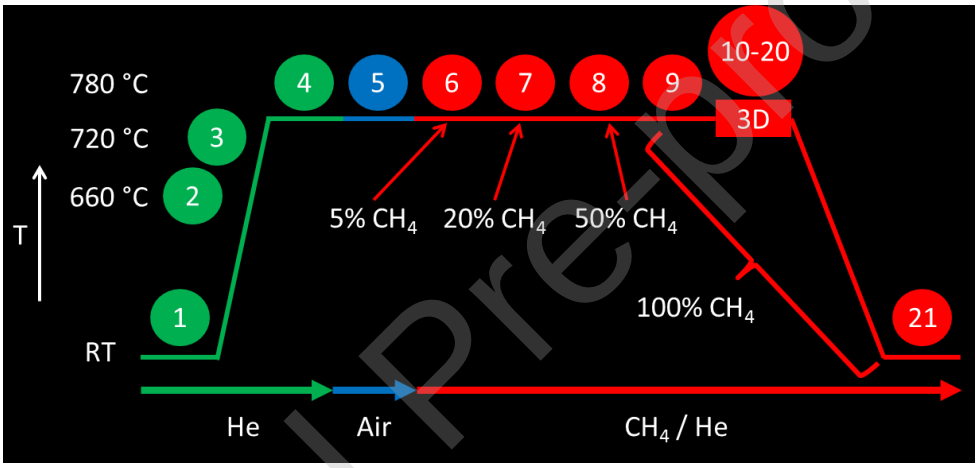

***Figure 1**: Schematic representation of the protocol followed during the OCM experiment with the BCFZ – 2%Mn-1.6%Na-3.1%W/SiO2 CMR.*

Initially, an XRD-CT scan of the CMR was performed at room temperature. In agreement with our previous study, the main crystalline phases present in the catalyst particles were cristobalite-low, tridymite-low, Mn_2O_3/Mn_7SiO_{12} and Na_2WO_4 (Figures S14, S15 and Table S3). The phase distribution maps shown in Figure 2 represent the (normalised) values of the scale factors of these crystalline phases as obtained from the Rietveld analysis of the CMR XRD-CT data collected at room temperature. It is seen that the two main crystalline SiO_2 phases, cristobalite and tridymite, are homogeneously distributed over the catalyst particles and define well their size and shape. On the other hand, it can be seen that there are certain areas have high concentration of Mn_2O_3/Mn_7SiO_{12}. Na_2WO_4 is present in all catalyst

Journal Pre-proof

particles but there are areas of high concentration of this phase too (i.e. hotspots). Finally, the phase distribution map of BCFZ demonstrates that the membrane wall thickness is fairly uniform (ca. 180-200 μm).

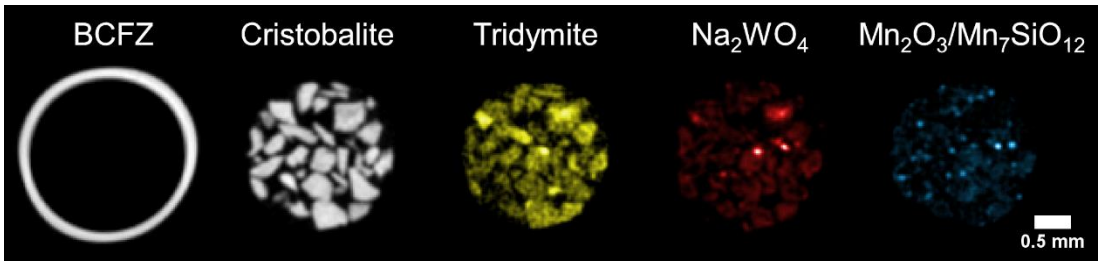

Figure 2: *Phase distribution maps created based on the values of the scale factors of the crystalline phases present in the CMR as obtained from the Rietveld analysis of the XRD-CT data collected at room temperature before the OCM experiment. From left to right: BCFZ, cristobalite (alpha - low-T), tridymite (alpha - low-T), Na_2WO_4 and Mn_2O_3/Mn_7SiO_{12}.*

The next XRD-CT scan was performed at 660 °C. Careful inspection of the reconstructed XRD-CT data revealed that the high temperature tomographic scans were performed at a seemingly different position compared to the room temperature scan; this is due to thermal expansion/movement of the CMR during heating. It was feasible to identify this vertical change of the probing position after the OCM experiment by comparing the phase distribution maps of cristobalite. As mentioned previously, the phase distribution maps of cristobalite define well the catalyst particles and can be used to correlate different tomographic datasets. As a result, the data of the high temperature XRD-CT scans cannot be directly compared with the room temperature XRD-CT scans. In Figure 3, the results from the high temperature XRD-CT scans are presented which are all at the same position (i.e. XRD-CT cross sections at a constant position of the CMR). The relative change of each phase, as determined from the integrated intensities (scale factors) for each XRD-CT dataset (i.e. integrated over the entire slice), is presented at the right side of Figure 3.

The support of the catalyst particles is seen to evolve at high temperatures which is in full agreement with the results obtained from our previous operando XRD-CT experiments of the catalytic membrane reactor with the same catalyst [68]. The diffraction peaks generated by Na_2WO_4 have disappeared completely at 660 °C

Journal Pre-proof

although its melting point is 695 °C in 1 bar pressure [77]. The mobile Na^+ species are incorporated into the SiO_2 framework and lead to the transformation of the remaining amorphous SiO_2 to the cristobalite phase. It can be seen though that after the initial spike, the diffraction signal corresponding to the cristobalite phase starts to decrease as it gradually transforms to the tridymite and quartz phases.

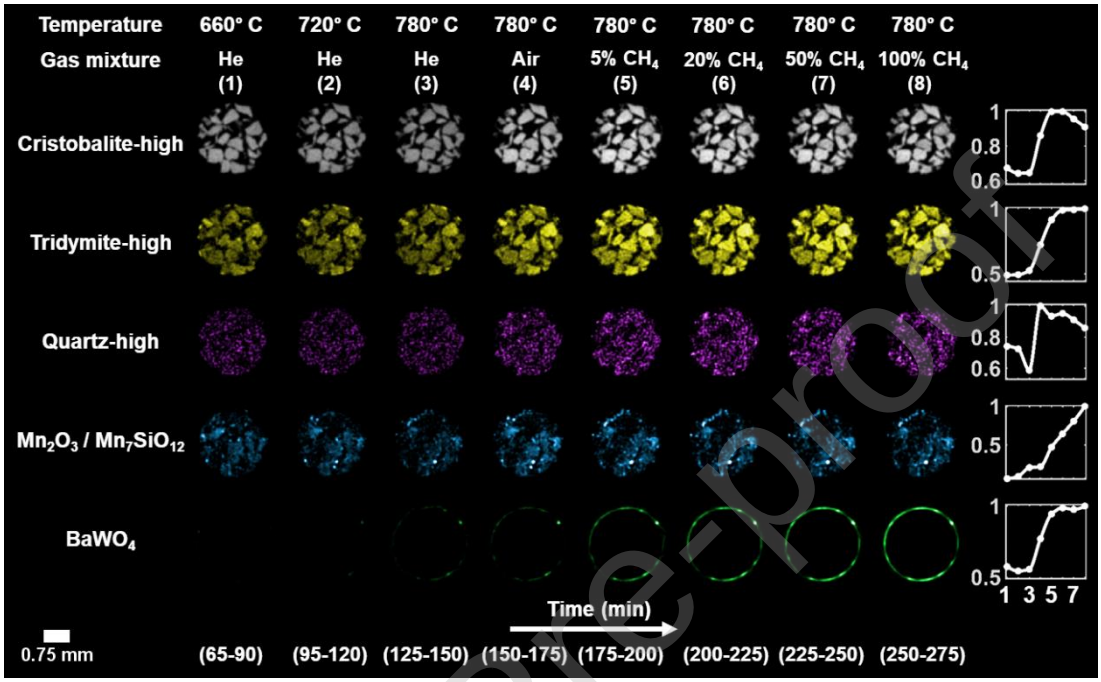

***Figure 3**: Phase distribution maps of Cristobalite (beta - high-T), Tridymite (beta - high-T), Quartz (beta - high-T), Mn_2O_3/Mn_7SiO_{12} and $BaWO_4$ at high temperatures during the OCM experiment. At the right side, the relative change of each phase, as determined from the integrated intensities for each XRD-CT dataset, is presented.*

The results from our previous work on the same CMR system showed that the crystalline Mn_2O_3/Mn_7SiO_{12} phase decreased with time at high temperatures when a gas mixture of 5% CH_4/He is used. However, it is shown in Figure 3 that letting air pass through the catalyst bed leads to a significant increase of the crystalline Mn_2O_3/Mn_7SiO_{12} phase under OCM operating temperatures (780 °C). This is important as, if Mn_2O_3/Mn_7SiO_{12} needs to be present under OCM conditions to yield an active and C_2+ selective catalyst, then an activation step by using air at high temperatures is necessary; an issue which has been raised before in literature [78]. In the past, the Mn-Na-W/SiO_2 catalysts have shown great stability in terms of CH_4 conversion but the selectivity towards C_2+ molecules has been shown to decrease

Journal Pre-proof

with time [79–81]. Therefore, it might be also necessary to switch the inlet gases from reaction mixture to air after many hours of operation at high temperatures as a regeneration step for the catalyst. For example, Hou et al. showed that treating the Mn-Na-W/SiO_2 catalyst with O_2 for 2 h at 800 °C led to the reappearance of Na_2WO_4 and Mn_2O_3/Mn_7SiO_{12} and the disappearance of $MnWO_4$ [82].

It should be emphasized though that such (regeneration) treatments may not be needed in CMRs containing Mn-Na-W/SiO_2 catalysts. In the BCFZ – 2 % Mn – 1.6 % Na – 3.1 % W/SiO_2 CMR (Figure 3), the diffraction signal generated by the Mn_2O_3/Mn_7SiO_{12} phase is seen to decrease under OCM reaction conditions (i.e. gas mixtures of CH_4/He) but the Mn_2O_3/Mn_7SiO_{12} to $MnWO_4$ phase transformation was not observed for the duration of the experiment. This is crucial as the catalyst bed was exposed to 100 % CH_4 for almost 10 h and the observed Mn_2O_3/Mn_7SiO_{12} phase(s) remained present till the end of the OCM experiment. This indicates that the O_2 transferred through the BCFZ ceramic membrane was enough to maintain the Mn_2O_3/Mn_7SiO_{12} phase(s) and prevent the bulk reduction of the Mn species (from Mn^{3+} to Mn^{2+}).

However, another crystalline WO_4^{2-}-containing phase appears as a result of the chemical interaction between the catalyst particles and the BCFZ ceramic membrane. This new phase is $BaWO_4$ and it is seen to form/grow at the inner side of the BCFZ membrane where the catalyst particles are in direct contact with the membrane. As it is shown in Figure 3, $BaWO_4$ continuously grows during the OCM experiment regardless of the applied chemical environment, proving that this is a purely temperature driven phenomenon.

3D-XRD-CT was also performed under OCM reaction conditions by collecting 11 XRD-CT datasets at different positions along the reactor (i.e. 25 μm apart) at 780 °C (flow rate of 100 ml min^{-1} of 100 % CH_4 at the inner side of the BCFZ membrane, through the catalyst bed). In Figure 4, the results from the volume rendering of the scale factors data volume (phase distribution volumes) are presented. The scale factors were normalised with respect to the maximum value for each data volume and the colour axes were scaled accordingly in order to improve the contrast of the respective figures (see also Figure S21).

Journal Pre-proof

The cristobalite phase distribution volume clearly describes the catalyst particles in terms of both size and shape. This is expected as cristobalite, being the main crystalline phase of the SiO_2 catalyst support, is homogeneously distributed (uniform distribution) over the particles. Tridymite is present in most catalyst particles but it can also be seen that the sample regions showing high tridymite concentration also correspond to low cristobalite concentration. Similarly to cristobalite, quartz is seen to be present in all catalyst particles albeit not as evenly distributed.

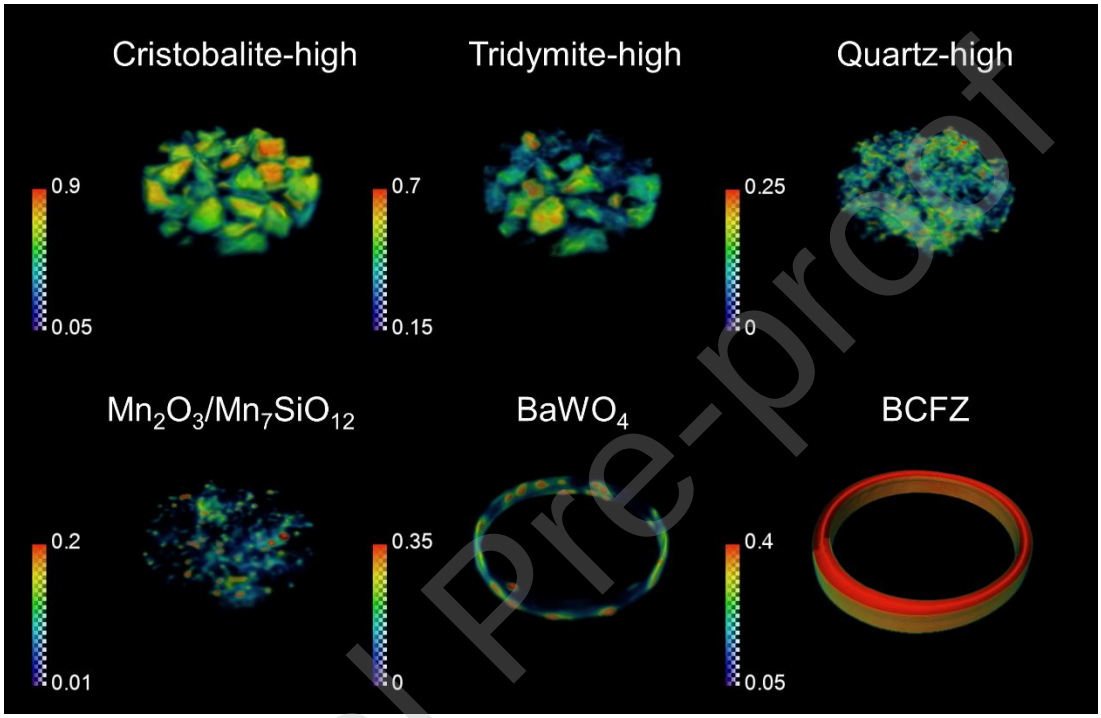

Figure 4: *Volume rendering of the normalised scale factors data volume (phase distribution volumes) obtained from the Rietveld analysis of the 3D-XRD-CT data. Top row: Cristobalite (beta - high-T), Tridymite (beta - high-T) and Quartz (beta - high-T). Bottom row: Mn_2O_3/Mn_7SiO_{12}, $BaWO_4$ and BCFZ. The values in the colorbar axes have been chosen to achieve the best possible contrast.*

The results obtained from the XRD-CT data collected at room temperature before the OCM experiment indicated that Mn_2O_3/Mn_7SiO_{12} is not homogeneously distributed over the catalyst particles but is only present at specific regions with very high concentration, mainly near the surface of the catalyst particles (Figure 2). The Mn_2O_3/Mn_7SiO_{12} phase distribution volume (Figure 4) serves to verify this result and also to show that the Mn_2O_3/Mn_7SiO_{12} distribution does not alter significantly under OCM reaction conditions.

Journal Pre-proof

The BCFZ membrane maintained its size and shape for the duration of the OCM experiment and no cracks were formed. This is also implied by the BCFZ phase distribution volume which clearly demonstrates the dense ceramic hollow-fibre design. Finally, the $BaWO_4$ phase distribution volume reveals that there are regions of high concentration of this phase at the inner side of the BCFZ membrane (hotspots of material) which, as it will be shown later, are mainly located at the catalyst-membrane interface. This is attributed to the W containing species, originating from the molten Na_2WO_4 phase, being both mobile and volatile.

Finally, it was feasible to directly compare the state of the catalyst before, during and after the OCM reaction. As mentioned previously, the CMR slightly moved during temperature ramping but fortunately one of the 3D-XRD-CT scans was at the same position as the one at ambient conditions before the OCM experiment. More importantly, the XRD-CT scan at room temperature after the OCM experiment is also at the same position allowing the direct comparison of these three datasets. The phase distribution maps presented Figure 5 correspond to the respective (normalised) phase scale factors obtained from the Rietveld analysis of the XRD-CT data.

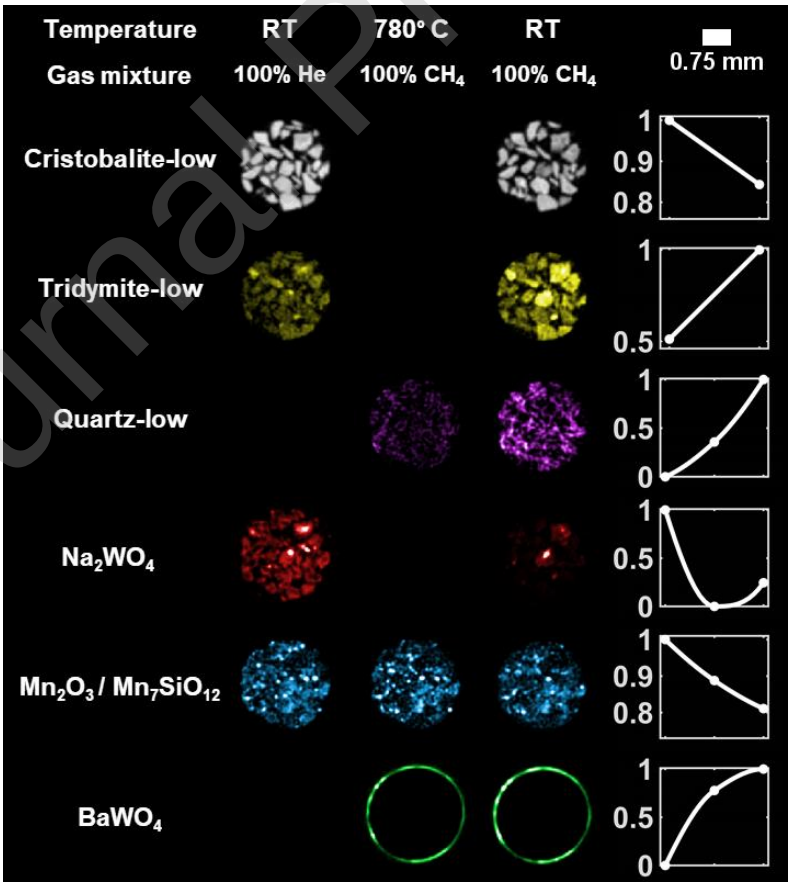

Journal Pre-proof

Figure 5: *Phase distribution maps of Cristobalite (alpha - low-T), Tridymite (alpha - low-T), Quartz (alpha - low-T), Na_2WO_4, Mn_2O_3/Mn_7SiO_{12} and $BaWO_4$ at room temperature before the OCM experiment, at high temperatures during the OCM experiment and at room temperature after the OCM experiment. At the right side, the relative change of each phase, as determined from the integrated intensities for each XRD-CT dataset, is presented.*

The comparison of these three XRD-CT datasets reveals that by the end of the OCM experiment, cristobalite has been partially consumed in favour of the growth of the tridymite and quartz phases. The Mn_2O_3/Mn_7SiO_{12} phase is also seen to decrease during this OCM experiment but the formation of the $MnWO_4$ phase was not observed. The Na_2WO_4 phase is seen to reform after cooling to room temperature albeit at a lesser extent (Figures S19-21). This is to be expected as $BaWO_4$ formed and continuously grew during the OCM experiment which was not present in the initial materials (i.e. catalyst and membrane) composing the CMR. The formation of $BaWO_4$ and the redistribution of the WO_4^{2-} species was also verified with complementary ex situ micro-CT and SEM/WDS measurements (Figures S22-23).

The spatially-resolved XRD patterns obtained from the XRD-CT data were not of high enough quality (i.e. in terms of number of observation points, angular resolution and signal-to-noise ratio) to allow for the refinement of structural parameters (i.e. thermal parameters and occupancy of the various atoms present in BCFZ). It was though possible to extract the scale factor and lattice parameter of BCFZ in a spatially-resolved manner and the results are presented in Figure 6. As mentioned previously, the BCFZ membrane retained its shape and size for the duration of the OCM experiment. However, as it is shown in Figure 6, Co is seen to gradually leave the BCFZ unit cell and be present as the crystalline CoO phase. It is still present as a minor phase/traces in the CMR XRD-CT data collected at room temperature after the OCM experiment but it raises questions regarding the long-term chemical stability of the BCFZ membrane under OCM reaction conditions and reducing chemical environments in general.

Journal Pre-proof

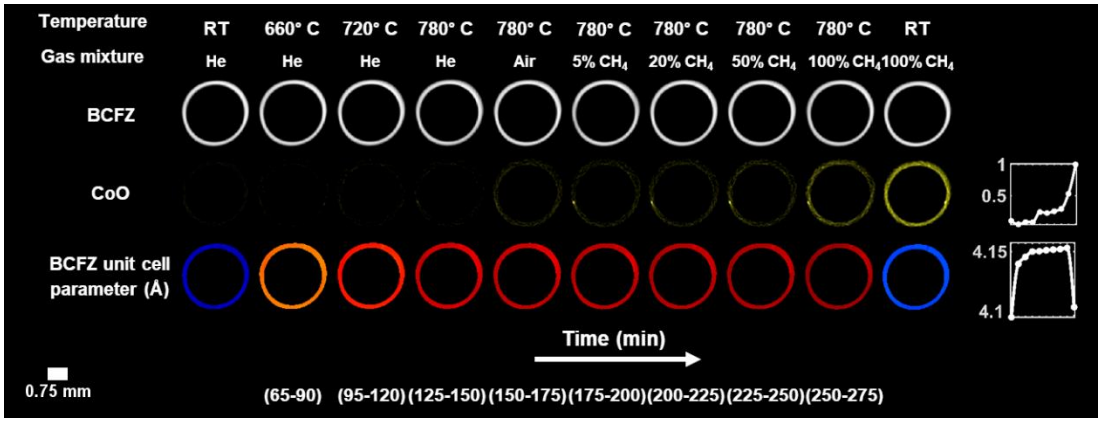

***Figure 6**: First and second row: Phase distribution maps of BCFZ and CoO. Third row: Maps corresponding to the BCFZ unit cell parameter during the OCM experiment.*

BCFZ membrane with La-Mn-Na-W/SiO_2 catalyst

As mentioned previously, the same experimental protocol was followed for all the operando CMR XRD-CT experiments (Figure 1). Initially, an XRD-CT scan of the BCFZ – 2 % La-2 % Mn-1.6 % Na-3.1 % W/SiO_2 CMR was performed at ambient conditions. The phase distribution maps of the various crystalline phases, as obtained from the Rietveld analysis (scale factors) of the XRD-CT data, are presented in Figure S28. The main difference between the La-promoted and the unpromoted catalyst lies in the distribution of the Mn_2O_3/Mn_7SiO_{12} phase as on the former it is seen to be homogeneously distributed.

The next three XRD-CT scans were performed at 660, 720 and 780 °C respectively. As in the case of the previous CMR experiment, inspection of the reconstructed XRD-CT data (cristobalite XRD-CT images) revealed that the high temperature XRD-CT scans were performed at a different position compared to the room temperature scan due to thermal expansion/movement of the CMR during heating. As a result, the XRD-CT data collected at high temperatures cannot/should not be directly compared with the XRD-CT data acquired at room temperature. The results from the Rietveld analysis of the high temperature XRD-CT data collected at the same position (i.e. XRD-CT cross sections at a constant position of the CMR) are presented in Figure 7. These phase distribution maps correspond to the values of the corresponding (normalized) scale factors, as obtained from the Rietveld analysis of the XRD-CT data. The relative change of each phase, as determined from the integrated intensities (i.e.

Journal Pre-proof

integrated over the entire slice) for each XRD-CT dataset, is presented at the right side of Figure 7.

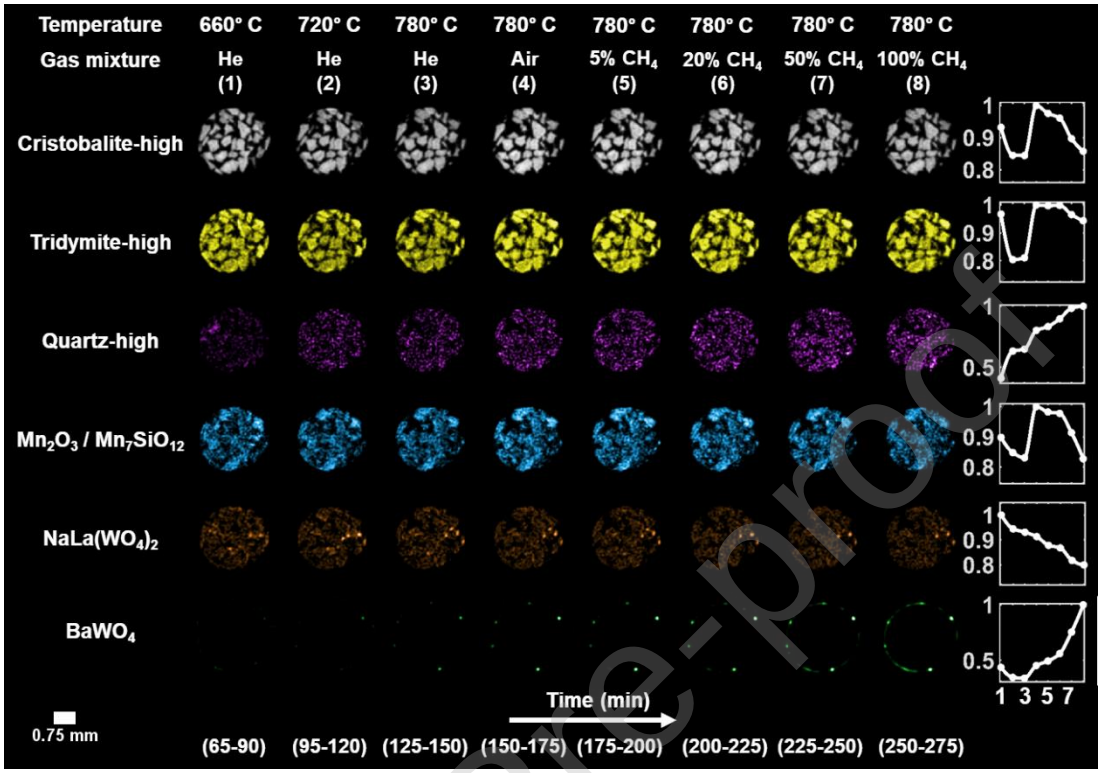

***Figure 7**: Phase distribution maps of Cristobalite (beta - high-T), Tridymite (beta - high-T), Quartz (beta - high-T), Mn_2O_3/Mn_7SiO_{12}, $NaLa(WO_4)_2$ and $BaWO_4$ at high temperatures during the OCM experiment. At the right side, the relative change of each phase, as determined from the integrated intensities for each XRD-CT dataset, is presented.*

There is an evolution of SiO_2 support at high temperatures; this phenomenon was thoroughly discussed previously and it is attributed to the presence of mobile Na+ species. The unexpected high concentrations of cristobalite and tridymite at 660 °C (compared to the other high temperature XRD-CT datasets) is explained by the fact that the CMR did not fully stabilize before reaching 780 °C. This can be seen after inspecting the cristobalite phase distribution maps presented in Figure 7 which suggest that the XRD-CT scan performed at 660 and 720 °C probed different positions of the CMR (i.e. with respect to all the XRD-CT data collected at 780 °C). The results obtained from the XRD-CT scans performed at the same position are though consistent with that which has been observed previously; namely that there is an

Journal Pre-proof

initial increase in the presence of cristobalite at 780 °C but that this is gradually consumed under OCM operating conditions while the tridymite and quartz phases increase as a function of time. The Mn_2O_3/Mn_7SiO_{12} phase is seen to increase in the presence of air which is also consistent with was observed in the BCFZ – 2 % Mn-1.6 % Na-3.1 % W/SiO_2 CMR. The concentration of the Mn_2O_3/Mn_7SiO_{12} phase is though seen to decrease with time under OCM reaction conditions, especially when CH_4 rich (i.e. > 20 % CH_4/He) reaction mixtures are used.

It can be seen that $BaWO_4$ is forming and growing only at specific regions (hotspots in Figure 7) where the catalyst particles are in direct contact with the BCFZ membrane. Only after for several hours of operation at high temperatures (each XRD-CT lasted approximately 45 min.) a uniform "ring" (layer) is observed at the inner BCFZ membrane wall. This delay could be attributed to the presence of the La species in the catalyst particles and specifically the $NaLa(WO_4)_2$ phase. It is indicated that the presence of this phase slows down the formation and growth of $BaWO_4$ compared to the unpromoted catalyst, by partially stabilising the mobile and volatile Na^+/WO_4^{2-} species. However, the slow decomposition of this newly formed phase at high temperatures was also observed. The delayed effect this phase had though suggests the solution to the formation of $BaWO_4$ phase lies on chemically trapping the volatile Na^+/WO_4^{2-} species.

As in the previous CMR experiment, 3D-XRD-CT was performed under OCM reaction conditions by collecting 10 XRD-CT cross sections at different positions along the reactor (i.e. 25 µm apart) at 780 °C (flow rate of 100 ml min-1 of 100 % CH4 at the inner side of the BCFZ membrane, through the catalyst bed). The phase distribution maps presented in Figure S29 correspond to the scale factors (normalised to the maximum value) as obtained from the Rietveld analysis of the 3D-XRD-CT data. As mentioned previously, these XRD-CT data should not be directly compared it as they correspond to different sample volumes. If the solid-state changes taking place in the CMR were only a function of position (spatial dependence only), then the observation points shown on the right side of Figure S29 should not follow any specific trend. These plots correspond to the summed intensity of the various scale factors (normalised to the maximum value) as obtained from the Rietveld analysis of the 3D-

Journal Pre-proof

XRD-CT data. However, for some crystalline phases there is a clear trend (even linear in some cases) indicating that some of the solid-state changes can be tracked as a function of time (temporal dependence). For example, it can be seen that cristobalite decreases with time while tridymite and quartz increase. More importantly though, there is a continuous growth of the $NaLa(WO_4)_2$ and $BaWO_4$ phases. This indicates that the formation/growth of $NaLa(WO_4)_2$ is not completely prevented by the formation/growth of $BaWO_4$. This is a key result as it implies that if the catalyst is thermally treated (e.g. extended calcination periods) prior to its insertion in the CMR in order to convert the Na_2WO_4 to $NaLa(WO_4)_2$, then the formation/growth of $BaWO_4$ could be potentially suppressed.

The results from the volume rendering of the scale factors data volume (phase distribution volumes) are presented in Figure 8. The scale factors were normalised with respect to the maximum value for each data volume and the colour axes were scaled accordingly in order to improve the contrast of the respective figures. As expected, the various crystalline SiO_2 phases are present in all catalyst particles. As expected, in contrast to the unpromoted catalyst (Figure 4), the Mn_2O_3/Mn_7SiO_{12} phase in the La-promoted catalyst is seen to be homogeneously distributed over all catalyst particles probed during the 3D-XRD-CT scan. The $BaWO_4$ phase is present in all XRD-CT datasets but it can also be observed that there are regions of high BaWO4 concentration (hotspots). These hotspots are located at the interface between the catalyst particles and the inner BCFZ membrane wall.

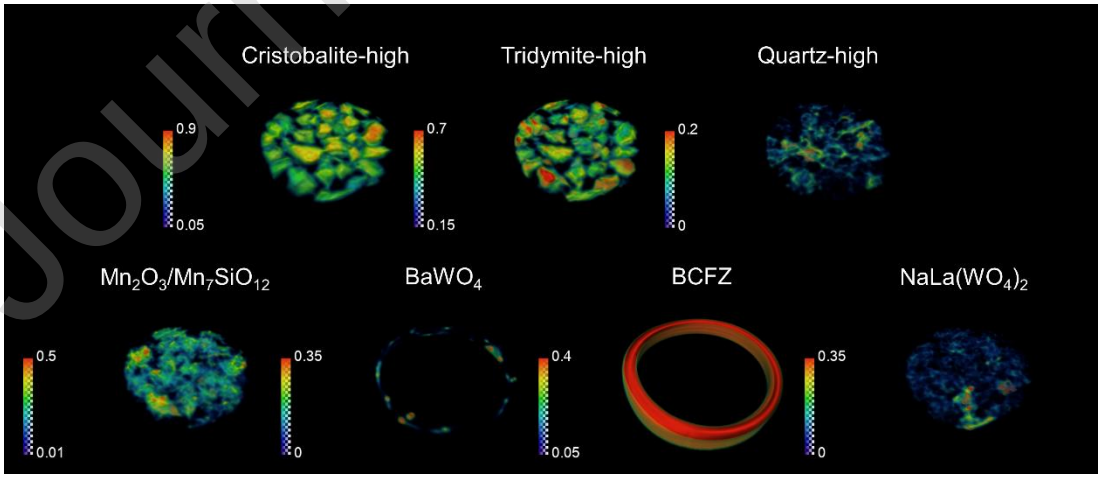

Journal Pre-proof

Figure 8: *Volume rendering of the normalised scale factors data volume (phase distribution volumes) obtained from the Rietveld analysis of the 3D-XRD-CT data. Top row: Cristobalite (beta - high-T), Tridymite (beta - high-T) and Quartz (beta - high-T). Bottom row: Mn_2O_3/Mn_7SiO_{12}, $BaWO_4$, BCFZand $NaLa(WO_4)_2$. The values in the colorbar axes have been chosen to achieve the best possible contrast.*

In contrast to the previous CMR experiment, the XRD-CT data acquired at room temperature after the OCM experiment did not probe the same sample volume as the XRD-CT data before the experiment (different position in the CMR). This means that these two datasets should not be directly compared in terms of quantitative analysis but can provide a good indication of the solid-state changes that took place in the CMR during the OCM experiment.

As in the case of the previous CMR, the BCFZ structure was also added to the Rietveld refinement and the results are presented in Figure S30. The maps corresponding to the BCFZ unit cell parameter are homogeneous and change only as a function of temperature. It should also be pointed out that shape and size of the BCFZ membrane did not change during the OCM experiment and no cracks were formed. However, the formation and growth of CoO is observed again showing that the results obtained from the previous CMR experiment are directly reproducible (Figure 6). Whilst the CoO is only a minor phase present in the diffraction patterns but it suggests there may be issues regarding the long-term chemical stability of BCFZ under OCM operating conditions.

In Figure 9, the phase distribution maps of various crystalline phases from the XRD-CT datasets are presented. These datasets correspond to the following XRD-CT scans: room temperature before the OCM experiment, at 780 °C under 100 % CH_4 flow (inner side of BCFZ membrane) and room temperature scan after the OCM experiment. It should be noted that the high temperature XRD-CT scan was performed at the same CMR position as the room temperature XRD-CT scan before the OCM experiment.

Journal Pre-proof

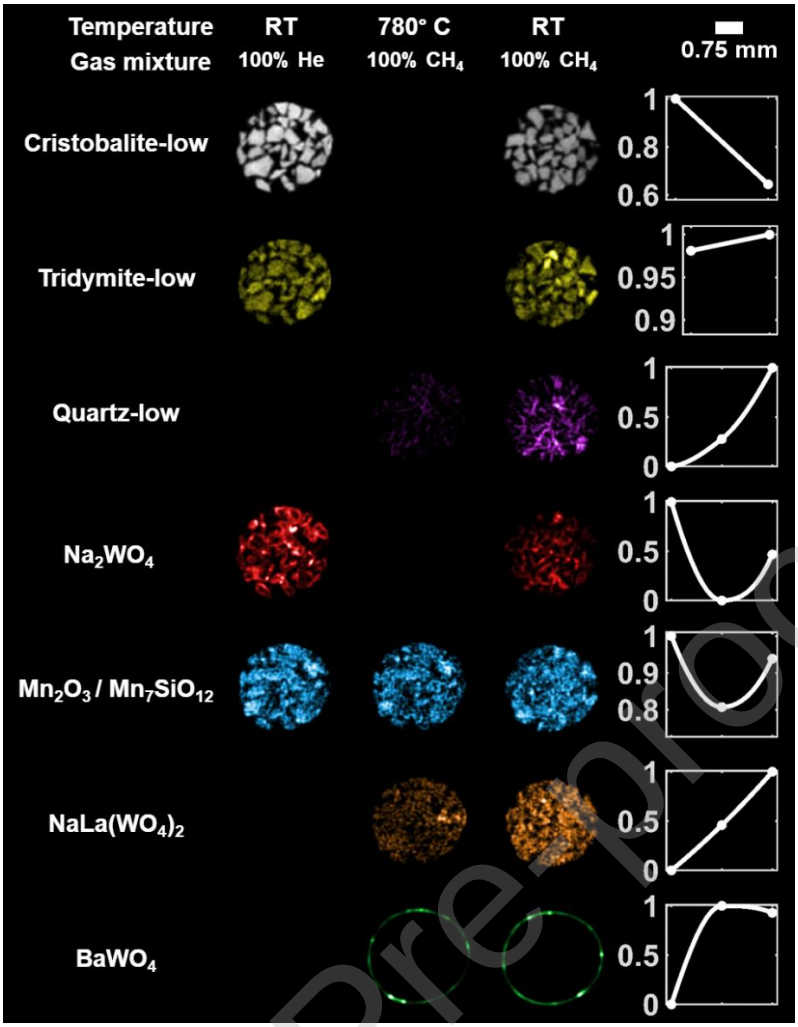

Figure 9: *Phase distribution maps of Cristobalite (alpha - low-T), Tridymite (alpha - low-T), Quartz (alpha - low-T), Na_2WO_4, Mn_2O_3/Mn_7SiO_{12}, $NaLa(WO_4)_2$ and $BaWO_4$ at room temperature before the OCM experiment, at high temperatures during the OCM experiment and at room temperature after the OCM experiment. At the right side, the relative change of each phase, as determined from the integrated intensities for each XRD-CT dataset, is presented.*

It can be seen that the evolution of the SiO_2 support is consistent with what has been observed in the previous CMR experiment (i.e. consumption of cristobalite and consequent growth of tridymite and quartz). As it is also shown in Figure S32, Na_2WO_4 reforms upon cooling to room temperature after the OCM experiment. Of course, the concentration of Na_2WO_4 is lower compared to the fresh catalyst as both $NaLa(WO_4)_2$ and $BaWO_4$ formed/grew during the operation of the CMR. The fact that the $NaLa(WO_4)_2$ phase was seen not only to form but also to increase at high temperatures in this CMR (Figure S32 and Figure 9) suggests that the $NaLa(WO_4)_2$ is chemically stable under these conditions. This means that not only the La species can

Journal Pre-proof

stabilise the mobile WO_4^{2-} species but it is also implied that if $NaLa(WO_4)_2$ is the only Na-W containing phase in the fresh catalyst (no Na_2WO_4) then the catalyst may be stable the formation/growth of $BaWO_4$ can be supressed and maybe even completely prevented.

LSCF membrane with La-Mn-Na-W/SiO_2 catalyst

The last CMR experiment was performed using a $La_{0.6}Sr_{0.4}Co_{0.2}Fe_{0.8}O_3$ (LSCF) membrane and the 2 % La-2 % Mn-1.6 % Na-3.1 % W/SiO_2 catalyst. The same experimental protocol was followed as in the other CMR experiments (Figure 1). Unfortunately, the quality of the LSCF – 2 % La-2 % Mn-1.6 % Na-3.1 % W/SiO_2 CMR data was significantly inferior compared to the other CMR data. More specifically, the raw diffraction data suffered from saturation (spottiness). This is clearly shown in Figure S33 where a summed 2D diffraction pattern derived from a line scan of the LSCF CMR XRD-CT data collected at room temperature is shown. Apart from the presence of large grains in the LSCF membrane that led to the formation of spots (single-crystal diffraction) on top of the powder diffraction data, the LSCF – La-Mn-Na-W/SiO_2 XRD-CT data severely suffered from self-absorption problems too (Figure S34).

The phase distribution maps of the various crystalline phases initially present in the CMR are shown in Figure S35. As in the previous two CMR experiments, the thermal expansion of the LSCF membrane resulted in probing different sample volumes at high temperatures compared to the room temperature XRD-CT scan. The results from the high temperature XRD-CT data, collected at the same position, are presented in Figure 11. The phase distribution maps shown in Figure 11 correspond to the values of the corresponding scale factors, normalised with respect to the maximum value, as obtained from the Rietveld analysis of these XRD-CT datasets (Figures S32-34). The relative change of each phase is plotted on the right side of Figure 11.

As expected, the cristobalite phase decreases with time at the high temperatures applied for the OCM experiment while tridymite is seen to be fairly stable and quartz significantly increases. As shown previously, the Mn_2O_3/Mn_7SiO_{12} phase is seen to

Journal Pre-proof

increase when air is used as the inlet gas mixture through the catalyst bed but then decreases with time under OCM reaction conditions.

It can be seen that in this CMR, although Ba is absent in the membrane material, there is chemical interaction between the catalyst particles and the LSCF membrane which leads to the formation and growth of a new phase, identified as $SrWO_4$. However, as in the case the second experiment (and in contrast to the first one), the $SrWO_4$ is primarily seen to form and grow only at specific regions (hotspots in Figure 11) where the catalyst particles are in direct contact with the LSCF membrane. This phenomenon, as described previously, was attributed to the presence of the $NaLa(WO_4)_2$ phase which partially stabilises the volatile Na^+/WO_4^{2-} species. It can be seen that the $SrWO_4$ phase increases with time at high temperatures, eventually forming a uniform layer at the inner LSCF membrane wall, as in the case of the $BaWO_4$ phase in the BCFZ CMRs. This is the key result of this experiment as it proves that the main drawback of the three CMRs is related to the unstable WO_4^{2-} species present at the catalyst at high temperatures.

Journal Pre-proof

Journal Pre-proof

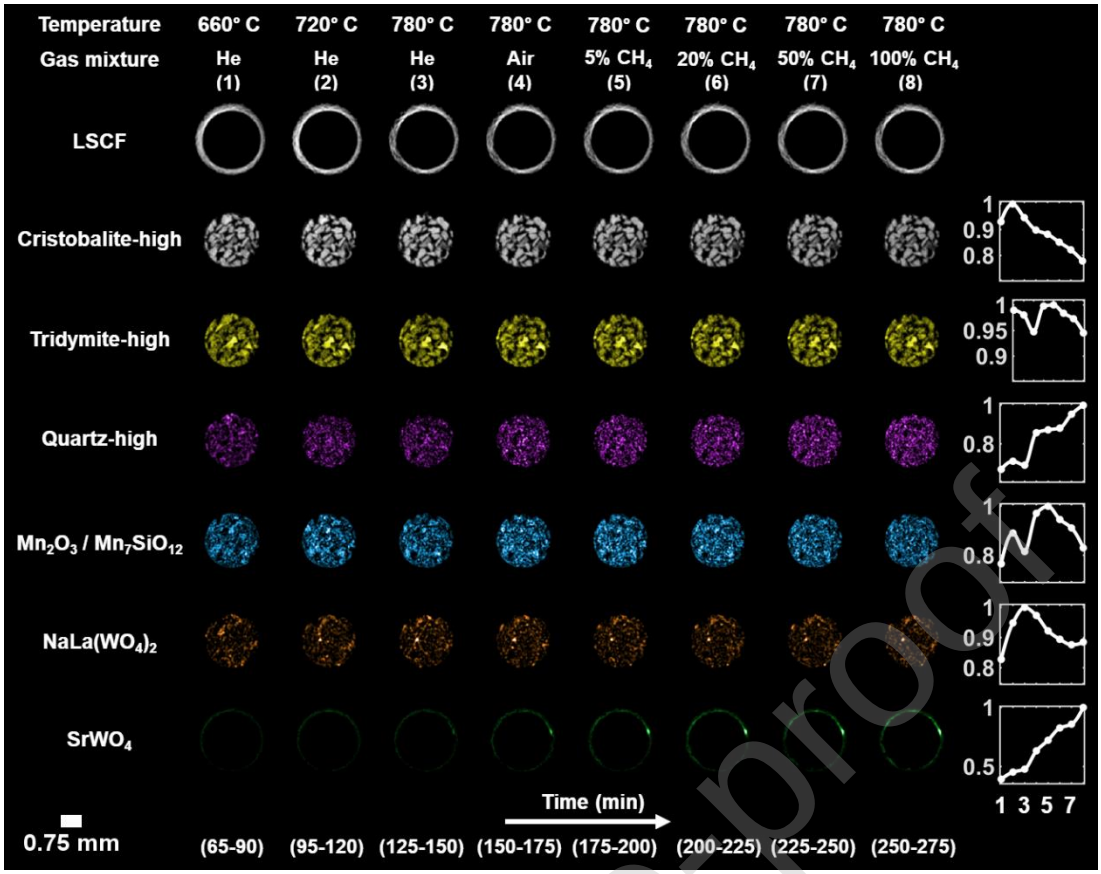

Figure 11: *Phase distribution maps of LSCF, Cristobalite (beta - high-T), Tridymite (beta - high-T), Quartz (beta - high-T), Mn_2O_3/Mn_7SiO_{12}, $NaLa(WO_4)_2$ and $SrWO_4$ at high temperatures during the OCM experiment. At the right side, the relative change of each phase, as determined from the integrated intensities for each XRD-CT dataset, is presented.*

As in the previous two CMR experiments, 3D-XRD-CT was also performed at 780 °C while maintaining the OCM reaction mixtures constant (100 ml min^{-1} of 100 % CH_4 at the inner side of the membrane through the catalyst bed and 100 ml min^{-1} air at the outer side of the LSCF membrane). The results from the Rietveld refinement of the 3D-XRD-CT data are presented in Figure S39. It can be seen that there is a continuous consumption of cristobalite and growth of quartz which is in full agreement with what has been observed in the previous experiments. It should also be noted that the $SrWO_4$ phase (Figure S39) is also seen to continuously grow as a function of time which is identical to the behaviour of the $BaWO_4$ phase in the BCFZ CMRs.

The results from the volume rendering of the 3D-XRD-CT data are presented in Figure 12. As expected, the three crystalline SiO_2 phases (cristobalite, tridymite and quartz) are homogeneously distributed over the catalyst particles. Similar is the case for the

Journal Pre-proof

Mn_2O_3/Mn_7SiO_{12} phase which is in full agreement with the results obtained from BCFZ CMR containing the same catalyst. The $NaLa(WO_4)_2$ phase is seen to be present in most catalyst particles indicating that the formation/growth of the $SrWO_4$ phase only delays but does not prevent its evolution.

It should be noted though that no cracks formed in the LSCF membrane and no other La, Sr, Co or Fe containing phases were observed during the OCM experiment (apart from the $SrWO_4$ phase). This is in contrast to what was observed in the BCFZ CMRs where the Co was seen to leave the BCFZ unit cell and form CoO. This result indicates that the LSCF membrane is more chemically stable under OCM reaction conditions compared to the BCFZ membrane.

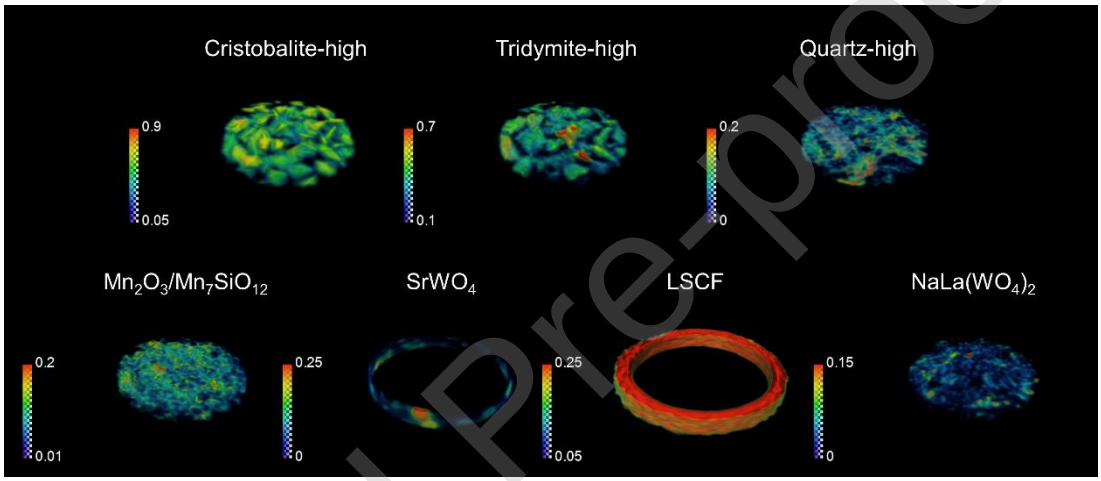

Figure 12: *Volume rendering of normalised the scale factors data volume (phase distribution volumes) obtained from the Rietveld analysis of the 3D-XRD-CT data. Top row: Cristobalite (beta - high-T), Tridymite (beta - high-T) and Quartz (beta - high-T). Bottom row: Mn_2O_3/Mn_7SiO_{12}, $SrWO_4$, LSCF and $NaLa(WO_4)_2$. The values in the colorbar axes have been chosen to achieve the best possible contrast.*

Finally, the results from the Rietveld analysis of three XRD-CT datasets collected at the same position are presented in Figure 13. These datasets correspond to XRD-CT data collected at room temperature before the OCM experiment, at 780 °C under 100 % CH_4 flow and at room temperature after the OCM experiment. In accordance to what was previously observed, cristobalite is seen to have been partially consumed by the end of the OCM experiment while tridymite and quartz have grown. The Mn_2O_3/Mn_7SiO_{12} phase is seen to decrease with time under OCM reaction conditions which in agreement with what has been previously observed (behaviour

Journal Pre-proof

of the La-promoted catalyst under OCM reaction conditions). The Na_2WO_4 is seen to be present at the room temperature XRD-CT scan after the OCM experiment. However, its concentration is significantly lower as both $SrWO_4$ and $NaLa(WO_4)_2$ formed and grew during the operation of the CMR (Figure S42).

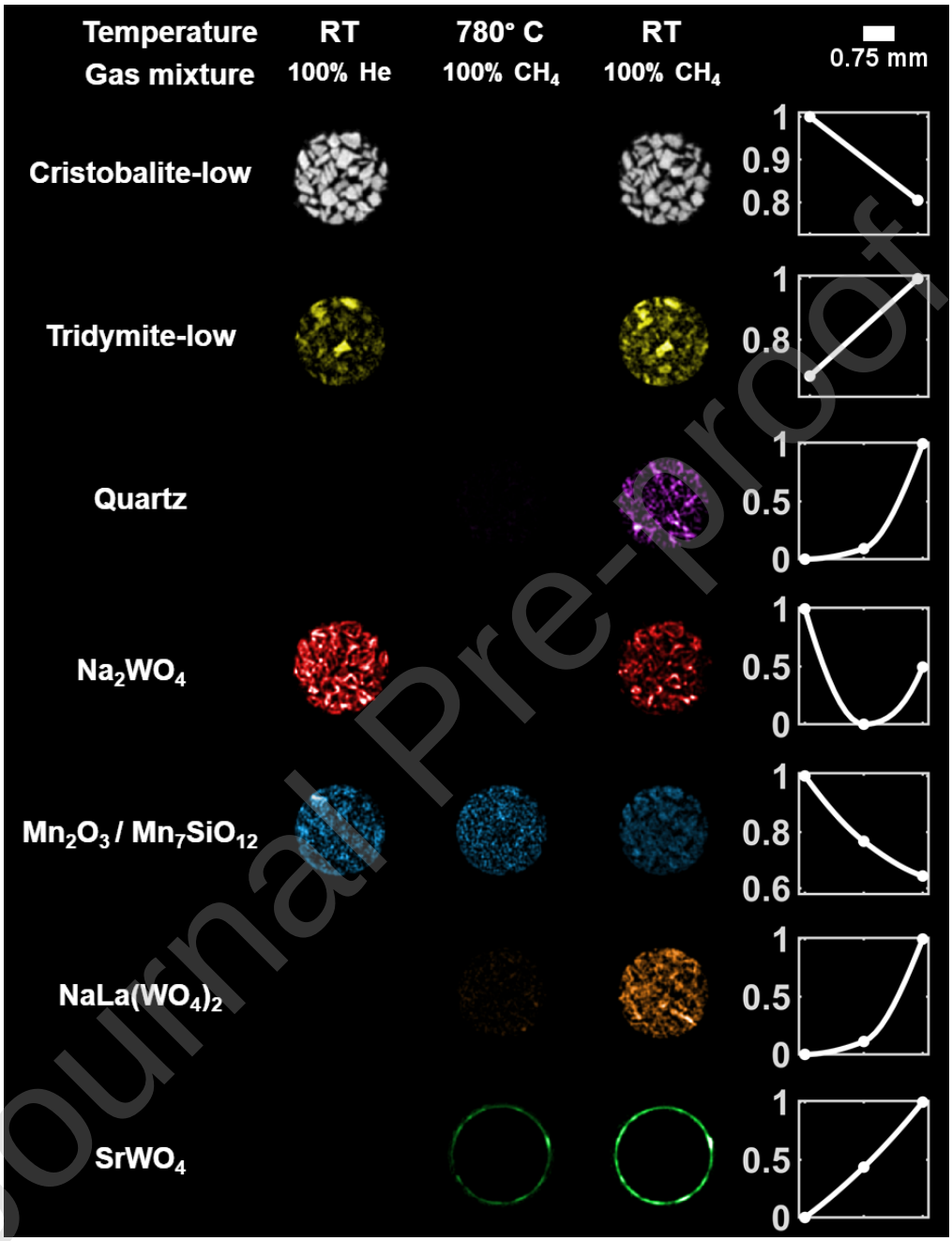

Figure 13: *Phase distribution maps of Cristobalite (alpha - low-T), Tridymite (alpha - low-T), Quartz (alpha - low-T), Na_2WO_4, Mn_2O_3/Mn_7SiO_{12}, $NaLa(WO_4)_2$ and $SrWO_4$ at room temperature before the OCM experiment, at high temperatures during the OCM experiment and at room temperature after the OCM experiment. At the right side, the relative change of each phase, as determined from the integrated intensities for each XRD-CT 'slice', is presented.*

Journal Pre-proof

Summary and Conclusions

Catalytic membrane reactors have the potential to render the process of oxidative coupling of methane to produce ethylene economically viable. For example, two of the highest values for C_2 yield (> 35 %) ever reported in literature have been achieved using catalytic membrane reactors [9,83]. However, a number of questions regarding the true state of the active catalyst/membrane and their stability over time remain unanswered. These integrated reactor systems are typically characterised ex situ with electron microscopy techniques (SEM/TEM/EDX) and bulk powder diffraction.

Herein, three different catalytic membrane reactor systems have been studied, for the first time, under real OCM reaction conditions with XRD-CT. The operando XRD-CT measurements allowed to spatially-resolve the pertinent changes in the chemical/physical state within all working CMRs. Despite the challenging nature of these experiments it has been shown that spatially-resolved diffraction information can be extracted from the interior of working catalytic membrane reactors. Indeed, the state of two different catalysts was captured prior to, under and after OCM operando conditions.

The three CMRs investigated under OCM operating conditions were a BCFZ – 2 % Mn-1.6 % Na-3.1 % W/SiO_2 CMR, a BCFZ – 2 % La-2 % Mn-1.6 % Na-3.1 % W/SiO_2 CMR and an LSCF – 2 % La-2 % Mn-1.6 % Na-3.1 % W/SiO_2 CMR. The three CMRs were operated under atmospheric pressure but future experiments could also investigate the impact of high pressure in the evolving chemistry of the various reactor components. It should be emphasized that no carbonate phases were observed under any imposed chemical environments (even under 100 % CH_4) for any CMR. It should also be pointed out that all three CMRs were captured in their active state where CO_2 is continuously produced as a side product of the OCM reaction. This is a very important result as it demonstrates that both BCFZ and LSCF are chemically stable under OCM reaction conditions and the produced CO_2 is not able to significantly damage the membranes; this is typically done through the formation of phases such as $BaCO_3$ and $SrCO_3$.

In all experiments, the Na_2WO_4 phase, present in the fresh catalysts, is seen to melt before reaching the required high temperatures for the OCM reaction (780 °C) and

Journal Pre-proof

coincident to this event the formation of a new phase is observed. In the BCFZ CMRs, this phase was identified as $BaWO_4$ while in the LSCF CMR the new phase was identified as $SrWO_4$. These new phases are seen to initially form at the interface between the catalyst particles and the inner side of the membranes. The mobility of W-containing species was independently confirmed by micro-CT and ex situ SEM/WDS measurements. These phases are seen to continuously grow under the high temperatures used for the OCM reaction and regardless of the chemical environment present (reaction mixtures used) indicating that their formation and subsequent growth is a purely temperature driven phenomenon. The growth of stable the $BaWO_4$ phase in the BCFZ CMRs and the $SrWO_4$ phase in the LSCF CMR is extremely important as:

(1) loss of the W-containing species is expected to have an impact on the stability of the catalyst (loss of one of the main catalyst components),

(2) it might lead to the deactivation of the membranes (BCFZ/LSCF) after many hours of operation by forming an inner layer at the membrane and therefore blocking the flow of oxygen to the catalyst bed

At this point it should be emphasized that in the La-promoted catalysts, the loss of WO_4^{2-} species and the formation/growth of $BaWO_4$/$SrWO_4$ did not prevent the formation of $NaLa(WO_4)_2$ in the catalyst particles. In fact, the $NaLa(WO_4)_2$ phase was seen to grow with time under OCM operating conditions (although with a delay compared to the respective fixed bed reactor experiments). This is important as the formation and subsequent growth of $NaLa(WO_4)_2$ suggests that if the catalyst if pre-treated before it is inserted in the CMR (e.g. extensive catalyst calcination periods), then the formation/growth of the $BaWO_4$/$SrWO_4$ can be suppressed if not completely prevented during the operation of the CMRs.

Regarding the catalyst behaviour, the SiO_2 support of both catalysts is also seen to evolve with time under OCM operating conditions. More specifically, cristobalite is seen to gradually transform to tridymite and then to quartz at high temperatures (780 °C). This phenomenon was attributed to the presence of mobile Na+ species and their incorporation to the SiO_2 framework. The Mn_2O_3/Mn_7SiO_{12} phase remains

Journal Pre-proof

present for the duration of the OCM experiments. The transformation of the Mn_2O_3/Mn_7SiO_{12} phase to the $MnWO_4$ phase was not observed in the Mn-Na-W/SiO_2 catalyst. This result suggests that the bulk reduction of the Mn species (Mn^{3+} to Mn^{2+}) was prevented in the CMRs. This observation becomes more important when it is taken into account that the 100 % CH_4 was used as the inlet gas to the catalyst bed for more than 8 h at 780 °C. This result implies that the oxygen permeation flux through the dense ceramic membranes was enough to prevent the bulk reduction of the Mn species present in the catalysts.

Last but not least, a crystal structure model of was created using high resolution neutron powder diffraction data collected at the ISIS neutron source. The model provided an opportunity to extract more information on the nature of the BCFZ membrane's performance in operation. The BCFZ structure was added to the Rietveld refinement model and it was shown that it was possible to create BCFZ phase distribution and lattice parameter maps. BCFZ has also been shown to be a promising electrode material for fuel cell applications and now a structure model is available for the fuel cell community. We expect that the structure model will be used in future studies to gain a better understanding of the performance of this material under different operating conditions (e.g. crystallographic properties as a function of temperature, chemical environment or potential).

Author Contributions

The OCM experiments were conceived by A.V., V.M., S.D.M.J. and A.M.B. M.D.M. and A.V. wrote the macros for the data acquisition and the scripts for the sinogram data pre-processing. A.V., D.M., P.S., S.D.M.J., S.W.P. and A.M.B. performed the OCM experiments. M.D.M. was responsible for ID15A instrumentation and setup at the ESRF. Data processing and analysis was performed by A.V. with assistance from M.D.M., S.D.M.J., D.M. and A.M.B. A.V. and S.D.M.J. developed the self-absorption correction algorithms. V.M. was responsible for the hollow-fibre dense ceramic membrane preparation and for the Scanning Electron Microscopy (SEM)/Energy Dispersive X-ray Spectrometry (EDS) sample preparation and measurement. P.C. was responsible for the BCFZ XAFS data analysis. C.L.B. was responsible the ISIS neutron powder diffraction data collection. The analysis of the BCFZ neutron powder

Journal Pre-proof

diffraction data was performed by A.V. with assistance from D.M., C.L.B., S.D.M.J. and A.M.B. A.V., D.M., S.D.M.J. and A.M.B. are responsible for writing the manuscript with feedback given by all contributors. A.M.B. directed the research.

Declaration of interests

The authors declare that they have no known competing financial interests or personal relationships that could have appeared to influence the work reported in this paper.

Acknowledgments

The development of the catalysts and membranes for the catalytic membrane reactor used in this work is funded within the DEMCAMER project as part of the European Union Seventh Framework Programme (FP7/2007-2013) under grant agreement no. NMP3-LA-2011-262840. Note: “The present publications reflect only the authors' views and the Union is not liable for any use that may be made of the information contained therein.” Antonis Vamvakeros and Dorota Matras (respectfully in full and in part) are supported through funding received from the European Union Horizon 2020 research and innovation programme under grant agreement no. 679933 (MEMERE project). The authors would like to thank the ESRF - The Europen Synchrotron for beamtime and CerPoTech AS for providing the ceramic powders. The authors would also like to thank Wilm Jones and Donato Decarolis for help with acquisition of the XAFS BCFZ data and the UK Catalysis Hub and the Diamond Light Source for the bag time at beamline B18. The authors would finally like to thank the ISIS neutron facilities for acquiring and providing the neutron powder diffraction data used in this work to model the BCFZ crystal structure.

Journal Pre-proof

References

[1] R.A. Kerr, Natural Gas From Shale Bursts Onto the Scene, Science (80-.). 328 (2010) 1624–1626. doi:10.1126/science.328.5986.1624.

[2] E. McFarland, Unconventional Chemistry for Unconventional Natural Gas, Science (80-.). 338 (2012) 340–342. doi:10.1126/science.1226840.

[3] I.E. Agency, Key World Energy Statistics 2019, 2019. doi:https://doi.org/https://doi.org/10.1787/71b3ce84-en.

[4] P. Tang, Q. Zhu, Z. Wu, D. Ma, Methane activation: the past and future, Energy Environ. Sci. 7 (2014) 2580–2591. doi:10.1039/C4EE00604F.

[5] H. Zimmermann, R. Walzl, Ethylene, in: Ullmann's Encycl. Ind. Chem., American Cancer Society, 2009. doi:10.1002/14356007.a10_045.pub3.

[6] G.E. Keller, M.M. Bhasin, Synthesis of ethylene via oxidative coupling of methane: I. Determination of active catalysts, J. Catal. 73 (1982) 9–19. doi:10.1016/0021-9517(82)90075-6.

[7] A. Cruellas, J.J. Bakker, M. van Sint Annaland, J.A. Medrano, F. Gallucci, Techno-economic analysis of oxidative coupling of methane: Current state of the art and future perspectives, Energy Convers. Manag. 198 (2019) 111789. doi:10.1016/J.ENCONMAN.2019.111789.

[8] A. Cruellas, T. Melchiori, F. Gallucci, M. van Sint Annaland, Oxidative Coupling of Methane: A Comparison of Different Reactor Configurations, Energy Technol. (2019) 1900148. doi:10.1002/ente.201900148.

[9] S. Bhatia, C.Y. Thien, A.R. Mohamed, Oxidative coupling of methane (OCM) in a catalytic membrane reactor and comparison of its performance with other catalytic reactors, Chem. Eng. J. 148 (2009) 525–532. doi:10.1016/J.CEJ.2009.01.008.

[10] W. Kiatkittipong, T. Tagawa, S. Goto, S. Assabumrungrat, K. Silpasup, P. Praserthdam, Comparative study of oxidative coupling of methane modeling in various types of reactor, Chem. Eng. J. 115 (2005) 63–71.

Journal Pre-proof

doi:10.1016/J.CEJ.2005.09.018.

[11] B.L. Farrell, S. Linic, Oxidative coupling of methane over mixed oxide catalysts designed for solid oxide membrane reactors, Catal. Sci. Technol. 6 (2016) 4370–4376. doi:10.1039/C5CY01622C.

[12] W. Wang, Y.S. Lin, Analysis of oxidative coupling of methane in dense oxide membrane reactors, J. Memb. Sci. 103 (1995) 219–233. doi:https://doi.org/10.1016/0376-7388(95)00005-W.

[13] A. Cruellas, T. Melchiori, F. Gallucci, M. van Sint Annaland, Advanced reactor concepts for oxidative coupling of methane, Catal. Rev. 59 (2017) 234–294. doi:10.1080/01614940.2017.1348085.

[14] Y. Liu, X. Tan, K. Li, Mixed Conducting Ceramics for Catalytic Membrane Processing, Catal. Rev. 48 (2006) 145–198. doi:10.1080/01614940600631348.

[15] S. Liu, X. Tan, K. Li, R. Hughes, METHANE COUPLING USING CATALYTIC MEMBRANE REACTORS, Catal. Rev. 43 (2001) 147–198. doi:10.1081/CR-100104388.

[16] W. Deibert, M.E. Ivanova, S. Baumann, O. Guillon, W.A. Meulenberg, Ion-conducting ceramic membrane reactors for high-temperature applications, J. Memb. Sci. 543 (2017) 79–97. doi:https://doi.org/10.1016/j.memsci.2017.08.016.

[17] Y. Wei, W. Yang, J. Caro, H. Wang, Dense ceramic oxygen permeable membranes and catalytic membrane reactors, Chem. Eng. J. 220 (2013) 185–203. doi:10.1016/J.CEJ.2013.01.048.

[18] Y. Teraoka, H.-M. Zhang, S. Furukawa, N. Yamazoe, OXYGEN PERMEATION THROUGH PEROVSKITE-TYPE OXIDES, Chem. Lett. 14 (1985) 1743–1746. doi:10.1246/cl.1985.1743.

[19] J. Sunarso, S. Baumann, J.M. Serra, W.A. Meulenberg, S. Liu, Y.S. Lin, J.C. Diniz da Costa, Mixed ionic–electronic conducting (MIEC) ceramic-based

Journal Pre-proof

membranes for oxygen separation, J. Memb. Sci. 320 (2008) 13–41. doi:https://doi.org/10.1016/j.memsci.2008.03.074.

[20] T. Schiestel, M. Kilgus, S. Peter, K.J. Caspary, H. Wang, J. Caro, Hollow fibre perovskite membranes for oxygen separation, J. Memb. Sci. 258 (2005) 1–4. doi:https://doi.org/10.1016/j.memsci.2005.03.035.

[21] X. Tan, K. Li, Inorganic hollow fibre membranes in catalytic processing, Curr. Opin. Chem. Eng. 1 (2011) 69–76. doi:https://doi.org/10.1016/j.coche.2011.08.004.

[22] S.J. Xu, W.J. Thomson, Perovskite-type oxide membranes for the oxidative coupling of methane, AIChE J. 43 (1997) 2731–2740. doi:10.1002/aic.690431319.

[23] A. Thursfield, I.S. Metcalfe, The use of dense mixed ionic and electronic conducting membranes for chemical production, J. Mater. Chem. 14 (2004) 2475–2485. doi:10.1039/B405676K.

[24] X. Dong, W. Jin, N. Xu, K. Li, Dense ceramic catalytic membranes and membrane reactors for energy and environmental applications, Chem. Commun. 47 (2011) 10886–10902. doi:10.1039/C1CC13001C.

[25] O. Czuprat, T. Schiestel, H. Voss, J. Caro, Oxidative Coupling of Methane in a BCFZ Perovskite Hollow Fiber Membrane Reactor, Ind. Eng. Chem. Res. 49 (2010) 10230–10236. doi:10.1021/ie100282g.

[26] L. Olivier, S. Haag, C. Mirodatos, A.C. van Veen, Oxidative coupling of methane using catalyst modified dense perovskite membrane reactors, Catal. Today. 142 (2009) 34–41. doi:https://doi.org/10.1016/j.cattod.2009.01.009.

[27] J.E. ten Elshof, B.A. van Hassel, H.J.M. Bouwmeester, Activation of methane using solid oxide membranes, Catal. Today. 25 (1995) 397–402. doi:https://doi.org/10.1016/0920-5861(95)00082-Q.

[28] J.E. ten Elshof, H.J.M. Bouwmeester, H. Verweij, Oxidative coupling of methane in a mixed-conducting perovskite membrane reactor, Appl. Catal. A

Journal Pre-proof

Gen. 130 (1995) 195–212. doi:https://doi.org/10.1016/0926-860X(95)00098-4.

[29] J. Tong, W. Yang, B. Zhu, R. Cai, Investigation of ideal zirconium-doped perovskite-type ceramic membrane materials for oxygen separation, J. Memb. Sci. 203 (2002) 175–189. doi:https://doi.org/10.1016/S0376-7388(02)00005-4.

[30] J. Luyten, A. Buekenhoudt, W. Adriansens, J. Cooymans, H. Weyten, F. Servaes, R. Leysen, Preparation of LaSrCoFeO3−x membranes, Solid State Ionics. 135 (2000) 637–642. doi:10.1016/S0167-2738(00)00425-2.

[31] S.J. Xu, W.J. Thomson, Stability of La0.6Sr0.4Co0.2Fe0.8O3-δ Perovskite Membranes in Reducing and Nonreducing Environments, Ind. Eng. Chem. Res. 37 (1998) 1290–1299. doi:10.1021/ie970761j.

[32] X. Tan, K. Li, Oxidative Coupling of Methane in a Perovskite Hollow-Fiber Membrane Reactor, Ind. Eng. Chem. Res. 45 (2006) 142–149. doi:10.1021/ie0506320.

[33] X. Tan, Z. Pang, Z. Gu, S. Liu, Catalytic perovskite hollow fibre membrane reactors for methane oxidative coupling, J. Memb. Sci. 302 (2007) 109–114. doi:https://doi.org/10.1016/j.memsci.2007.06.033.

[34] H. Wang, C. Tablet, W. Yang, J. Caro, In situ high temperature X-ray diffraction studies of mixed ionic and electronic conducting perovskite-type membranes, Mater. Lett. 59 (2005) 3750–3755. doi:https://doi.org/10.1016/j.matlet.2005.06.067.

[35] H. Wang, C. Tablet, J. Caro, Oxygen production at low temperature using dense perovskite hollow fiber membranes, J. Memb. Sci. 322 (2008) 214–217. doi:https://doi.org/10.1016/j.memsci.2008.05.038.

[36] O. Czuprat, M. Arnold, S. Schirrmeister, T. Schiestel, J. Caro, Influence of CO2 on the oxygen permeation performance of perovskite-type BaCoxFeyZrzO3−δ hollow fiber membranes, J. Memb. Sci. 364 (2010) 132–137. doi:https://doi.org/10.1016/j.memsci.2010.08.019.

Journal Pre-proof

[37] K. Efimov, O. Czuprat, A. Feldhoff, In-situ X-ray diffraction study of carbonate formation and decomposition in perovskite-type BCFZ, J. Solid State Chem. 184 (2011) 1085–1089. doi:https://doi.org/10.1016/j.jssc.2011.03.023.

[38] L. Yang, Z. Wu, W. Jin, N. Xu, Structure and Oxygen Permeability of BaCo0.4Fe0.6-xZrxO3-δ Oxide: Effect of the Synthesis Method, Ind. Eng. Chem. Res. 43 (2004) 2747–2752. doi:10.1021/ie049977t.

[39] C. Tablet, G. Grubert, H. Wang, T. Schiestel, M. Schroeder, B. Langanke, J. Caro, Oxygen permeation study of perovskite hollow fiber membranes, Catal. Today. 104 (2005) 126–130. doi:https://doi.org/10.1016/j.cattod.2005.03.064.

[40] M.G. O'Brien, A.M. Beale, S.D.M. Jacques, M. Di Michiel, B.M. Weckhuysen, Closing the operando gap: The application of high energy photons for studying catalytic solids at work, Appl. Catal. A Gen. 391 (2011) 468–476. doi:10.1016/J.APCATA.2010.06.027.

[41] R. Portela, S. Perez-Ferreras, A. Serrano-Lotina, M.A. Bañares, Engineering operando methodology: Understanding catalysis in time and space, Front. Chem. Sci. Eng. 12 (2018) 509–536. doi:10.1007/s11705-018-1740-9.

[42] J.-D. Grunwaldt, J.B. Wagner, R.E. Dunin-Borkowski, Imaging Catalysts at Work: A Hierarchical Approach from the Macro- to the Meso- and Nano-scale, ChemCatChem. 5 (2013) 62–80. doi:10.1002/cctc.201200356.

[43] N.E. Tsakoumis, A.P.E. York, D. Chen, M. Rønning, Catalyst characterisation techniques and reaction cells operating at realistic conditions; towards acquisition of kinetically relevant information, Catal. Sci. Technol. 5 (2015) 4859–4883. doi:10.1039/C5CY00269A.

[44] A. Urakawa, Trends and advances in Operando methodology, Curr. Opin. Chem. Eng. 12 (2016) 31–36. doi:https://doi.org/10.1016/j.coche.2016.02.002.

[45] F. Meirer, B.M. Weckhuysen, Spatial and temporal exploration of heterogeneous catalysts with synchrotron radiation, Nat. Rev. Mater. 3

Journal Pre-proof

(2018) 324–340. doi:10.1038/s41578-018-0044-5.

[46] A.M. Beale, S.D.M. Jacques, E.K. Gibson, M. Di Michiel, Progress towards five dimensional diffraction imaging of functional materials under process conditions, Coord. Chem. Rev. 277–278 (2014) 208–223. doi:https://doi.org/10.1016/j.ccr.2014.05.008.

[47] S.D.M. Jacques, M. Di Michiel, A.M. Beale, T. Sochi, M.G. O'Brien, L. Espinosa-Alonso, B.M. Weckhuysen, P. Barnes, Dynamic X-Ray Diffraction Computed Tomography Reveals Real-Time Insight into Catalyst Active Phase Evolution, Angew. Chemie Int. Ed. 50 (2011) 10148–10152. doi:10.1002/anie.201104604.

[48] M.G. O'Brien, S.D.M. Jacques, M. Di Michiel, P. Barnes, B.M. Weckhuysen, A.M. Beale, Active phase evolution in single Ni/Al2O3 methanation catalyst bodies studied in real time using combined μ-XRD-CT and μ-absorption-CT, Chem. Sci. 3 (2012) 509–523. doi:10.1039/C1SC00637A.

[49] T.L. Sheppard, S.W.T. Price, F. Benzi, S. Baier, M. Klumpp, R. Dittmeyer, W. Schwieger, J.-D. Grunwaldt, In Situ Multimodal 3D Chemical Imaging of a Hierarchically Structured Core@Shell Catalyst, J. Am. Chem. Soc. 139 (2017) 7855–7863. doi:10.1021/jacs.7b02177.

[50] H. Matsui, N. Ishiguro, T. Uruga, O. Sekizawa, K. Higashi, N. Maejima, M. Tada, Operando 3D Visualization of Migration and Degradation of a Platinum Cathode Catalyst in a Polymer Electrolyte Fuel Cell, Angew. Chemie Int. Ed. 56 (2017) 9371–9375. doi:10.1002/anie.201703940.

[51] A.M. Beale, S.D.M. Jacques, M. Di Michiel, F.W. Mosselmans, S.W.T. Price, P. Senecal, A. Vamvakeros, J. Paterson, X-ray physico-chemical imaging during activation of cobalt-based fischer-tropsch synthesis catalysts, Philos. Trans. R. Soc. A Math. Phys. Eng. Sci. 376 (2018). doi:10.1098/rsta.2017.0057.

[52] A. Vamvakeros, S.D.M. Jacques, M. Di Michiel, D. Matras, V. Middelkoop, I.Z. Ismagilov, E.V. Matus, V.V. Kuznetsov, J. Drnec, P. Senecal, A.M. Beale, 5D operando tomographic diffraction imaging of a catalyst bed, Nat. Commun. 9

Journal Pre-proof

(2018) 4751. doi:10.1038/s41467-018-07046-8.

[53] D. Matras, S.D.M. Jacques, H.R. Godini, M. Khadivi, J. Drnec, A. Poulain, R.J. Cernik, A.M. Beale, Real-Time Operando Diffraction Imaging of La–Sr/CaO During the Oxidative Coupling of Methane, J. Phys. Chem. C. 122 (2018) 2221–2230. doi:10.1021/acs.jpcc.7b11573.

[54] Y. De Vos, A. Vamvakeros, D. Matras, M. Jacobs, P. Van Der Voort, I. Van Driessche, S. Jacques, V. Middelkoop, A. Verberckmoes, Sustainable iron-based oxygen carriers for hydrogen production – Real-time operando investigation, Int. J. Greenh. Gas Control. 88 (2019). doi:10.1016/j.ijggc.2019.06.016.

[55] D. Matras, S.D.M. Jacques, S. Poulston, N. Grosjean, C. Estruch Bosch, B. Rollins, J. Wright, M. Di Michiel, A. Vamvakeros, R.J. Cernik, A.M. Beale, Operando and Postreaction Diffraction Imaging of the La-Sr/CaO Catalyst in the Oxidative Coupling of Methane Reaction, J. Phys. Chem. C. 123 (2019) 1751–1760. doi:10.1021/acs.jpcc.8b09018.

[56] T. Li, T.M.M. Heenan, M.F. Rabuni, B. Wang, N.M. Farandos, G.H. Kelsall, D. Matras, C. Tan, X. Lu, S.D.M. Jacques, D.J.L. Brett, P.R. Shearing, M. Di Michiel, A.M. Beale, A. Vamvakeros, K. Li, Design of next-generation ceramic fuel cells and real-time characterization with synchrotron X-ray diffraction computed tomography, Nat. Commun. 10 (2019). doi:10.1038/s41467-019-09427-z.

[57] V. Middelkoop, A. Vamvakeros, D. de Wit, S.D.M. Jacques, S. Danaci, C. Jacquot, Y. de Vos, D. Matras, S.W.T. Price, A.M. Beale, 3D printed Ni/Al2O3 based catalysts for CO2 methanation - a comparative and operando XRD-CT study, J. CO2 Util. 33 (2019) 478–487. doi:https://doi.org/10.1016/j.jcou.2019.07.013.

[58] T. Saida, O. Sekizawa, N. Ishiguro, M. Hoshino, K. Uesugi, T. Uruga, S. Ohkoshi, T. Yokoyama, M. Tada, 4D Visualization of a Cathode Catalyst Layer in a Polymer Electrolyte Fuel Cell by 3D Laminography–XAFS, Angew. Chemie

Journal Pre-proof

Int. Ed. 51 (2012) 10311–10314. doi:10.1002/anie.201204478.

[59] S.D.M. Jacques, M. Di Michiel, S.A.J. Kimber, X. Yang, R.J. Cernik, A.M. Beale, S.J.L. Billinge, Pair distribution function computed tomography, Nat. Commun. 4 (2013) 2536. doi:10.1038/ncomms3536.

[60] E.K. Gibson, M.W. Zandbergen, S.D.M. Jacques, C. Biao, R.J. Cernik, M.G. O'Brien, M. Di Michiel, B.M. Weckhuysen, A.M. Beale, Noninvasive Spatiotemporal Profiling of the Processes of Impregnation and Drying within Mo/Al2O3 Catalyst Bodies by a Combination of X-ray Absorption Tomography and Diagonal Offset Raman Spectroscopy, ACS Catal. 3 (2013) 339–347. doi:10.1021/cs300746a.

[61] D.S. Wragg, M.G. O'Brien, M. Di Michiel, F. Lonstad-Bleken, Rietveld analysis of computed tomography and its application to methanol to olefin reactor beds, J. Appl. Crystallogr. 48 (2015) 1719–1728. https://doi.org/10.1107/S1600576715017288.

[62] S.W.T. Price, K. Ignatyev, K. Geraki, M. Basham, J. Filik, N.T. Vo, P.T. Witte, A.M. Beale, J.F.W. Mosselmans, Chemical imaging of single catalyst particles with scanning μ-XANES-CT and μ-XRF-CT, Phys. Chem. Chem. Phys. 17 (2015) 521–529. doi:10.1039/C4CP04488F.

[63] S.W.T. Price, K. Geraki, K. Ignatyev, P.T. Witte, A.M. Beale, J.F.W. Mosselmans, In Situ Microfocus Chemical Computed Tomography of the Composition of a Single Catalyst Particle During Hydrogenation of Nitrobenzene in the Liquid Phase, Angew. Chemie. 127 (2015) 10024–10027. doi:10.1002/ange.201504227.

[64] S.W.T. Price, D.J. Martin, A.D. Parsons, W.A. Sławiński, A. Vamvakeros, S.J. Keylock, A.M. Beale, J.F.W. Mosselmans, Chemical imaging of Fischer-Tropsch catalysts under operating conditions, Sci. Adv. 3 (2017). doi:10.1126/sciadv.1602838.

[65] P. Senecal, S.D.M. Jacques, M. Di Michiel, S.A.J. Kimber, A. Vamvakeros, Y. Odarchenko, I. Lezcano-Gonzalez, J. Paterson, E. Ferguson, A.M. Beale, Real-

Journal Pre-proof

Time Scattering-Contrast Imaging of a Supported Cobalt-Based Catalyst Body during Activation and Fischer-Tropsch Synthesis Revealing Spatial Dependence of Particle Size and Phase on Catalytic Properties, ACS Catal. 7 (2017). doi:10.1021/acscatal.6b03145.

[66] U. Kleuker, P. Suortti, W. Weyrich, P. Spanne, Feasibility study of x-ray diffraction computed tomography for medical imaging, Phys. Med. Biol. 43 (1998) 2911–2923. doi:10.1088/0031-9155/43/10/017.

[67] G. Harding, J. Kosanetzky, U. Neitzel, X-ray diffraction computed tomography, Med. Phys. 14 (1987) 515–525. doi:10.1118/1.596063.

[68] A. Vamvakeros, S.D.M. Jacques, V. Middelkoop, M. Di Michiel, C.K. Egan, I.Z. Ismagilov, G.B.M. Vaughan, F. Gallucci, M. Van Sint Annaland, P.R. Shearing, R.J. Cernik, A.M. Beale, Real time chemical imaging of a working catalytic membrane reactor during oxidative coupling of methane, Chem. Commun. 51 (2015) 12752–12755. doi:10.1039/c5cc03208c.

[69] I. Ismagilov, E. Matus, M. Kerzhentsev, I. Prosvirin, R. Navarro, J. Fierro, G. Gerritsen, E. Abbenhuis, Z. Ismagilov, Design of Highly Efficient Catalyst for Rational Way of Direct Conversion of Methane, Eurasian Chem. J. 17 (2015). doi:10.18321/ectj201.

[70] I.Z. Ismagilov, E. V Matus, S.D. Vasil'ev, V. V Kuznetsov, M.A. Kerzhentsev, Z.R. Ismagilov, Oxidative condensation of methane in the presence of modified MnNaW/SiO2 catalysts, Kinet. Catal. 56 (2015) 456–465. doi:10.1134/S0023158415040096.

[71] J. Van Noyen, V. Middelkoop, C. Buysse, A. Kovalevsky, F. Snijkers, A. Buekenhoudt, S. Mullens, J. Luyten, J. Kretzschmar, S. Lenaerts, Fabrication of perovskite capillary membranes for high temperature gas separation, Catal. Today. 193 (2012) 172–178. doi:https://doi.org/10.1016/j.cattod.2012.03.005.

[72] V. Middelkoop, H. Chen, B. Michielsen, M. Jacobs, G. Syvertsen-Wiig, M. Mertens, A. Buekenhoudt, F. Snijkers, Development and characterisation of

Journal Pre-proof

Journal Pre-proof

dense lanthanum-based perovskite oxygen-separation capillary membranes for high-temperature applications, J. Memb. Sci. 468 (2014) 250–258. doi:https://doi.org/10.1016/j.memsci.2014.05.032.

[73] A. Vamvakeros, S.D.M. Jacques, M. Di Michiel, V. Middelkoop, C.K. Egan, R.J. Cernik, A.M. Beale, Removing multiple outliers and single-crystal artefacts from X-ray diffraction computed tomography data, J. Appl. Crystallogr. 48 (2015). doi:10.1107/S1600576715020701.

[74] M.A. Newton, S. Checchia, A.J. Knorpp, D. Stoian, W. van Beek, H. Emerich, A. Longo, J.A. van Bokhoven, On isothermality in some commonly used plug flow reactors for X-ray based investigations of catalysts, Catal. Sci. Technol. 9 (2019) 3081–3089. doi:10.1039/C9CY00464E.

[75] A. Coelho, TOPAS and TOPAS-Academic: an optimization program integrating computer algebra and crystallographic objects written in C++, J. Appl. Crystallogr. 51 (2018) 210–218. https://doi.org/10.1107/S1600576718000183.

[76] MATLAB, (n.d.).

[77] R.W. Goranson, F.C. Kracek, An Experimental Investigation of the Effect of Pressure on Phase Equilibria of Sodium Tungstate and of Related Thermodynamic Properties, J. Chem. Phys. 3 (1935) 87–92. doi:10.1063/1.1749613.

[78] T.P. Tiemersma, M.J. Tuinier, F. Gallucci, J.A.M. Kuipers, M. van S. Annaland, A kinetics study for the oxidative coupling of methane on a Mn/Na2WO4/SiO2 catalyst, Appl. Catal. A Gen. 433–434 (2012) 96–108. doi:https://doi.org/10.1016/j.apcata.2012.05.002.

[79] D.J. Wang, M.P. Rosynek, J.H. Lunsford, Oxidative Coupling of Methane over Oxide-Supported Sodium-Manganese Catalysts, J. Catal. 155 (1995) 390–402. doi:https://doi.org/10.1006/jcat.1995.1221.

[80] S. Pak, J.H. Lunsford, Thermal effects during the oxidative coupling of methane over Mn/Na2WO4/SiO2 and Mn/Na2WO4/MgO catalysts, Appl.

Journal Pre-proof

Catal. A Gen. 168 (1998) 131–137. doi:https://doi.org/10.1016/S0926-860X(97)00340-2.

[81] Y. Kou, B. Zhang, J. Niu, S. Li, H. Wang, T. Tanaka, S. Yoshida, Amorphous Features of Working Catalysts: XAFS and XPS Characterization of Mn/Na2WO4/SiO2as Used for the Oxidative Coupling of Methane, J. Catal. 173 (1998) 399–408. doi:10.1006/JCAT.1997.1900.

[82] S. Hou, Y. Cao, W. Xiong, H. Liu, Y. Kou, Site Requirements for the Oxidative Coupling of Methane on SiO2-Supported Mn Catalysts, Ind. Eng. Chem. Res. 45 (2006) 7077–7083. doi:10.1021/ie060269c.

[83] N.H. Othman, Z. Wu, K. Li, An oxygen permeable membrane microreactor with an in-situ deposited Bi1.5Y0.3Sm0.2O3−δ catalyst for oxidative coupling of methane, J. Memb. Sci. 488 (2015) 182–193. doi:10.1016/J.MEMSCI.2015.04.027.

Journal Pre-proof